Light Water Reactor Sustainability Program

Assessment of Radiation Resistance of Selected Alloys in The ARRM Program Using Ion Irradiation

September 30, 2016

U.S. Department of Energy

Office of Nuclear Energy

M3LW-16OR0406024

Assessment of Radiation Resistance of Selected Alloys in The ARRM Program Using Ion Irradiation

Gary S. Was, Miao Song, Mi Wang
University of Michigan

Prepared for the
U.S. Department of Energy
Office of Nuclear Energy

SUMMARY

This report summarizes the research activities during the period September 2014 to September 2016, with the objective of assessing the radiation resistance of several commercial alloys. Alloys including alloy 625, alloy 625Plus, alloy 625 Direct Aged (DA), alloy 725, Types 310, alloy 316, alloy 800 and alloy 690 and T92 were irradiated over this period. The report will focus on the as received microstructure, irradiated microstructure, irradiation hardening and irradiation assisted stress corrosion cracking (IASCC) of these alloys.

The two primary objectives of the advanced radiation resistant materials (ARRM) program are as follows: First, by 2022, to identify and test a degradation resistant alloy, which lies within current commercial alloy specifications. Second, by 2024, to develop and test a new advanced alloy with superior degradation resistance. This two-pronged approach will ensure that a code qualified, radiation resistant material is available for use by vendors and utilities in the near term and will also allow extensive testing to be performed on new advanced materials to ensure their superior performance to very high dose levels.

Alloys were first pre-characterized to document the microstructure of the as-received condition. They were then irradiated with 2 MeV protons to 5 dpa at 360°C and at a damage rate of ~1 x 10^{-5} dpa/s. Characterization of the irradiated samples included irradiation hardening, phase stability, dislocation loop microstructure radiation induced segregation and IASCC susceptibility. The IASCC susceptibility was measured using constant extension rate tensile (CERT) tests in either BWR Normal Water Chemistry (NWC) or PWR primary water to several percent plastic strain. Characterization of the cracking on the irradiated surface relative to the unirradiated area was used to assess the resistance to IASCC.

The major outcomes of the program during this year include:

- The chemical composition and heat treatment had a significant impact on the microstructure of as-received materials of nickel base alloys.
- The as-received materials were generally homogenous at multiscale levels as determined by various pre-characterization techniques.
- Alloy 690 and alloy 725 exhibited lowest susceptibility of formation of long range order phase in nickel rich alloy, which includes alloy 625, 625Plus, alloy 625DA, alloy 725 and alloy 690. Alloy 310 exhibited lower susceptibility of formation of gamma prime phase compared with alloy 800. No irradiation induced or enhanced precipitates were identified in alloy 316L.
- Voids were observed in alloys 310 and 316L.
- Little irradiation hardening was observed in T92. Significant hardening was observed in alloy 316L, 800, while the nickel base alloys show moderate hardening.
- Significant radiation induce segregation was identified in all the nickel base alloys.
- Among the high-strength alloys, alloy 625DA was the most susceptible to IASCC in both NWC and primary water environments.
- Among the low strength alloys, alloy 625 was much more susceptible to IASCC than a reference alloy (austenitic stainless steel Type 304) in BWR NWC environment.
- IASCC susceptibility was higher in BWR NWC for most of the alloys, only alloy 625 had a greater IASCC susceptibility in PWR primary water than in BWR NWC environment.

From the irradiation hardening perspective, alloy T92 showed the lowest irradiation hardening. Alloy 725 exhibited better phase stability among the high strength alloys examined thus far. Alloys 310 and

316L showed poor void swelling resistance. Alloys 625 and 625DA show high susceptibility to the formation of long range order phase.

All of the high strength alloys, 625Plus, 625DA, and 725, exhibited large increases in IASCC susceptibility following proton irradiation to 5 dpa. For the low strength alloys, alloy 625 exhibited very high IASCC susceptibility at a dose of 5 dpa in both BWR NWC and PWR primary water environments. A predominant microstructural feature has yet to be identified as the cause of the poor IASCC performance.

CONTENTS

FIGURES

TABLES

1. INTRODUCTION

The life extension of current existing reactors and design of next generation nuclear reactors require advanced materials that can maintain structural integrity in harsh radiation environments. Over the past years, Electric Power Research Institute (EPRI) has conducted a systematic approach for identifying all possible degradation mechanisms and their potential effects on the reactor components. Void swelling, stress corrosion cracking (SCC), irradiation assisted stress corrosion cracking (IASCC) and fracture toughness are the major concerns at high levels of radiation damage. However, most in-core structures consist of austenitic stainless steels, which are susceptible to degradation at a relatively low dose. Thus, replacement of these components may become a necessity.

The Advanced Radiation Resistant Materials (ARRM) program was created to address these issues. The ARRM project is aimed at identifying promising candidate alloys that can replace austenitic stainless steels, which suffer from serious irradiation-assisted stress corrosion cracking in light water reactors environments. If suitable replacement materials can be identified, reactors can operate with better efficiency and lower costs of maintenance and repair. The ARRM Program is jointly funded by EPRI, The Department of Energy and Bechtel Marine Propulsion Corp.

The core of ARRM project is to identify the materials with good resistant to irradiation assisted stress corrosion cracking (IASCC), then the candidate materials will be further examined by the neutron radiation. IASCC describes the stress corrosion cracking process of materials that can be significantly accelerated in the present of irradiation. It is identified as one of the primary degradation mechanisms of core components made of stainless steels and nickel-base alloys, which are applied as fuel cladding, control rods blade, neutron source tubes, baffle bolts, springs in light water reactors (LWRs) systems [1-4]. The similar degradation is also expected in Supercritical Water Reactor (SCWR), which is a promising concept for Gen IV nuclear reactors [5, 6]. For a given material, the IASCC susceptibility is known to be controlled by stress state, corrosive media, microstructure and irradiation dose, which may be a combination of effects rather than a sole factor [7].

In practice, austenitic stainless steels used in core components have proved to be problematic, especially as the irradiation dose goes higher [8-10]. The fracture toughness of Type304L SS was extremely low even after 4 dpa irradiation [11]. Void swelling may become significant at higher dose [12]. More importantly, IASCC may occur at a much early life during service [11]. The nickel-base alloys X750 and 718 show generally good performance in LWRs with a few failures that may result in plant outages[13]. However, these failures are costly and necessitate materials reselection for the life extension of LWRs.

The two primary objectives of the ARRM program are as follows: First, by 2022, to identify and test a degradation resistant alloy, which lies within current commercial alloy specifications. Second, by 2024, to develop and test a new advanced alloy with superior degradation resistance. This two-pronged approach will ensure that a code qualified, radiation resistant material is available for use by vendors and utilities in the near term and will also allow extensive testing to be performed on new advanced materials to ensure their superior performance to very high dose levels.

The candidate alloys were selected based on the weighted score and the state of knowledge of all the potential candidate materials included commercial alloys as well as novel materials such as ultrafine grained materials and metallic glasses, etc., with consideration of both low strength (Figure 1) and high strength (Figure 2) applications. The alloys selected as potential high strength materials include alloy 625Plus, alloy 625DA, alloy 725 and 14YWT ODS steel. The alloys chosen for low strength application include alloy 625, T91, alloy 690, alloy 800, alloy 310, C22 and Zr-2.5Nb. The test matrix also includes 316L and X-750 as control alloys for low strength and high-strength applications, respectively.

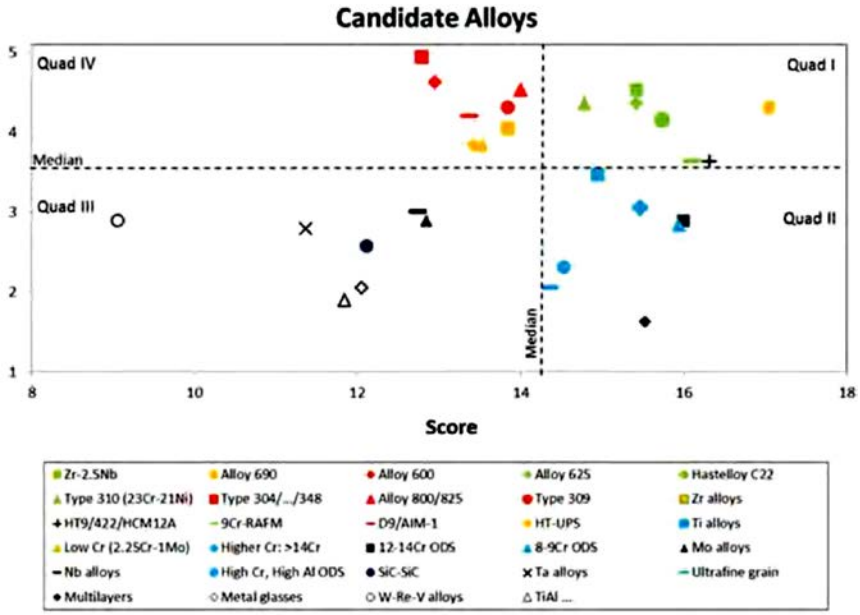

Figure 1. The weighted score and state of knowledge of alloys for potential low strength applications [11].

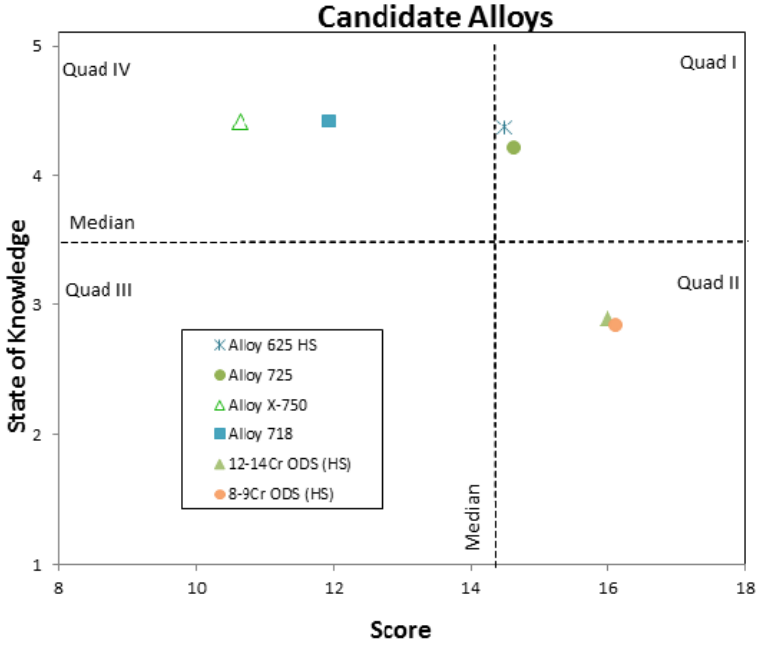

Figure 2. The weighted score and state of knowledge of alloys for potential high strength applications [11].

2. EXPERIMENTAL

2.1 Materials and Specimens

2.1.1 Alloys

Several groups of materials were tested including nickel base alloy, austenitic stainless steel, ferrtic/martensitic (F/M) steel. The nickel base alloy tested includes alloy 690 and alloy 625 family. The alloy 625 family was tested including several versions of alloy 625 and its derivative alloy 725 during the first year of this project. Alloy 625 was examined in three heat treatment conditions of different heats. Alloy 625 is solution treated at 955°C for 0.5h followed by water quenching. Alloy 625Plus is heat treated as follows; solution heat treated at 1038°C for 2h, fan cooling, then aging at 725°C for 8h, cooled at 56°C/hr to 621°C for another 8h ageing, then air cooled to room temperature. 625DA is 625 plus direct aging after hot working at a temperature range of 648-667°C for a duration of 81h then air cooling to room temperature. Although within the alloy 625 specification, these three 625 heats show slightly different chemical compositions. For alloy 625Plus, the addition of Ti is similar to that of alloy 725, which is around 5 times the original weight percentage of that in alloy 625. Alloy 725 follows the same heat treatment recipe as alloy 625Plus. Among these alloys, alloy 625 is tested as a low strength application while the other three alloys are precipitation hardened and designed for high-strength applications. Austenitic stainless steel includes alloy 316L and alloy 310. Alloy 316L is a control material for the the low strength materials. Incoloy 800 was also selected to be examined as one of the candidate for low strength application. Grade 92 or T92 was the only F/M steel that tested in the program. The chemical compositions are detailed in Table 1.

Table 1. Chemical compositions of alloys investigated (wt.%)

Alloy	Ni	Cr	Mo	Fe	Nb	Ti	Al	Ta	C	Si	Mn	Co	P	S	Cu	Mg	B	W	V	N
625	61.02	22.38	8.77	3.51	3.57	.23	.17	.02	.04	.08	.06	.03	.002	.001	-	-	-			
625DA	62.41	20.76	8.39	3.88	3.58	.31	.33	.03	.036	.06	.08	.05	.009	.0004	.05	.0039	.0023			
625Plus	60.38	20.99	8.02	Bal.	3.4	1.28	.2	-	.008	.03	.02	-	.001	.0005	-	-	-			
725	57.60	21.52	8.07	7.94	3.41	1.35	.17	.01	.011	.04	.04	.02	.004	.0006	.01	-	.0032			
690	59.33	29.44	0.01	10.38	0.01	0.35	.23		.03	.05	0.15	.009		0.001		.001				.01
316L	10.11	16.20	2.06	Bal.		.002	.009	.017	.017	.35	1.58	.17	.036	.001	.37					.08
310	19.26	24.21	.01	Bal.					.059	.69	1.3	.01	.005	.001						.058
800	32.21	20.21	.3	44.9		.44	.24		.01	.45	.82	.079	.017	.0002	.24					
T92	.12	8.81	.36	Bal.	.08	.01	.01		.0091	.1	.4		.005	.0005	.01			1.78	.18	.046

2.1.2 Samples

Tensile and TEM samples were fabricated from the materials made by the standard design used for proton irradiations at the Michigan Ion Beam Laboratory (MIBL) at the University of Michigan. All the samples were machined with the tensile axis oriented in the extrusion direction. The tensile samples have a square gage section of 2 mm, a gage length of 21 mm and threaded ends, see Figure 3. The TEM samples are also rectangular, 20 mm long with a square section of 2 mm, as shown in Figure 3. Before using in any experiments, all the samples were mechanically polished with silicon carbide abrasive paper from 360 to 4000 grit then electropolished to obtain a mirror finish.

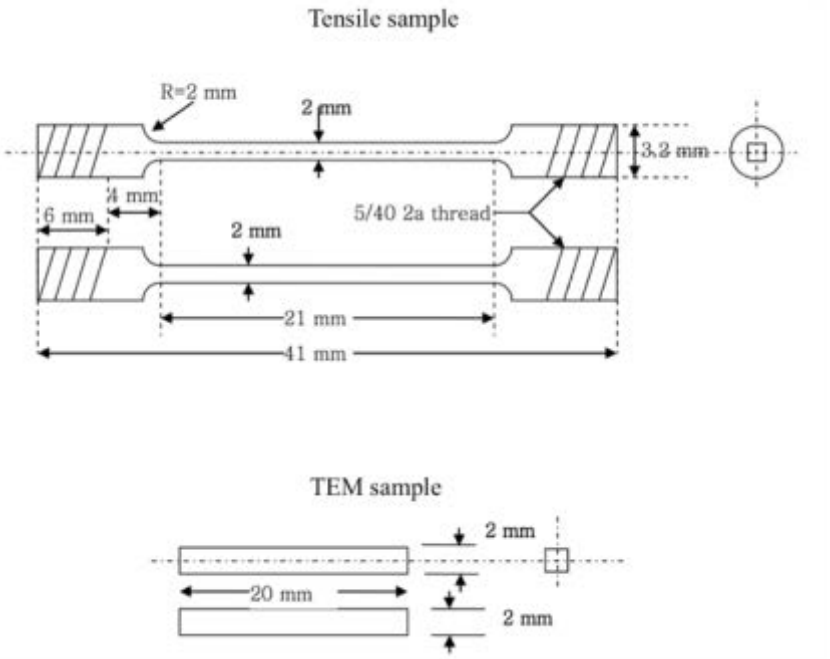

Figure 2. Schematic diagram of tensile sample (top) and TEM sample (bottom).

2.2 Sample Preparation for Microstructure Characterization

Specimens with dimensions of 2 × 2× 20 mm were cut from the as-received (AR) billet using electro discharge machine (EDM). The samples for optical observation were prepared by mechanical grinding up to 800 grid followed by cloth polishing with 1 μm diamond paste. Vibration polishing was performed after cloth polishing. The nickel base alloys were electrically etched in a solution of 10g citric acid plus 10g ammonium sulfate in 1L water. The current density was around 0.01A/cm^2. The finished samples exhibited a dull gold color. Electron backscatter diffraction (EBSD) specimens were prepared by the same procedure as those specimens for optical observation with the last step of electro-polishing instead of electro-etching. The electrolyte solution for 625 family nickel base alloy was a 20vol.% sulfuric acid in methanol solution. The polishing was performed at -40°C at a voltage around 20V for 30s. All the other alloys (T92, 310, 316L, 800, 690) were polished by a 10% perchloric acid 90% methanol solution with voltage of 30V for 30s. The disks for transmission electron microscopy (TEM) experiments were prepared by mechanical grinding of 3 mm disks down to tens of μm. The disks were then perforated in a TenuPol-5 twinjet polisher with the same solution of the one for electropolishing. The irradiated samples are prepared by back thinning of the un-irradiated side to a thickness of around 60 μm with fine grid sand paper to avoid mechanical deformation of the specimens. The irradiated side was then electropolished to the depth at which observations would be made (typically ~ 10μm). Polishing time was determined from a polishing curve collected beforehand. The as-ground disks were back thinned by twin jet polisher until perforation. Scanning electron microscope (SEM) experiments were performed using an FEI Helios 650 nanolab system equipped with both energy-dispersive X-ray (EDX) spectroscopy and EBSD detectors. The electron backscattering detection (EBSD) maps were collected with an operating voltage of 20kV and a working distance of 15 mm. The step size for EBSD collection was typically around 1 μm. TEM experiments were performed using JEOL 2010F and JEOL 3011 microscopes operated at 200 kV and 300 kV, respectively.

2.3 Irradiation Experimental Conditions

The proton irradiation experiments were conducted using a 3 MV NEC Tandem accelerator in the Michigan Ion Beam Laboratory (MIBL) at the University of Michigan. Four tensile samples and three TEM samples were irradiated on a specially designed stage, as shown in Figure 4. One TEM sample on each side of the stage served as the guide sample and was not fully irradiated. Four thermocouples were welded on the guide samples, used for calibrating the temperature of the samples. The irradiation area was about 16 mm wide and 8 mm long therefore, only the central part of the samples was irradiated. Both ends of the samples were positioned outside of the irradiation area. A schematic diagram of the stage design is illustrated in Figure 5. The cross-sectional view of the stage is shown in Figure 6, which shows a heater and an air cooling loop beneath the copper block, which were used to control the temperature of the samples.

Irradiations were conducted with 2 MeV protons at a dose rate of about 1.3×10^{-5} dpa/s. The dose and dose rate were estimated using SRIM 2013 (full cascade option) [14]. The resulting damage layer was approximately 20 microns with relatively uniform damage in the first 15 microns. An example of damage profile (Alloy 725) is shown in Figure 7.

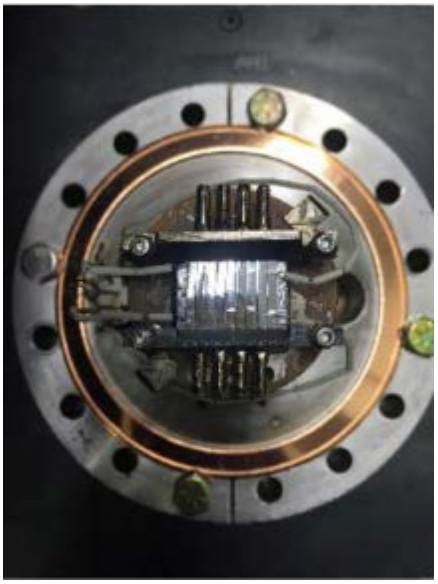

Figure 4. Photo of an irradiation stage with tensile and TEM samples (example: Alloy 725 irradiated to 5 dpa).

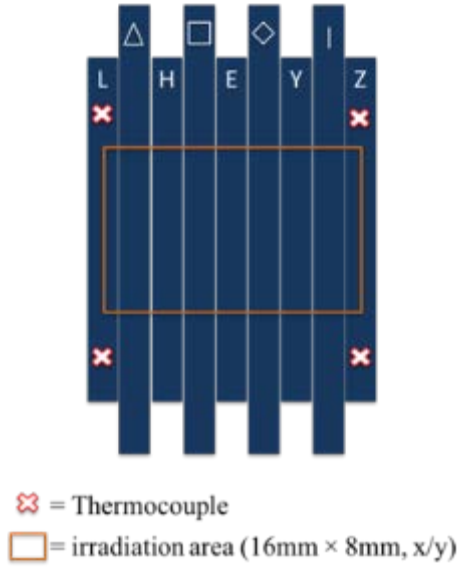

Figure 5. Schematic diagram of the irradiation stage.

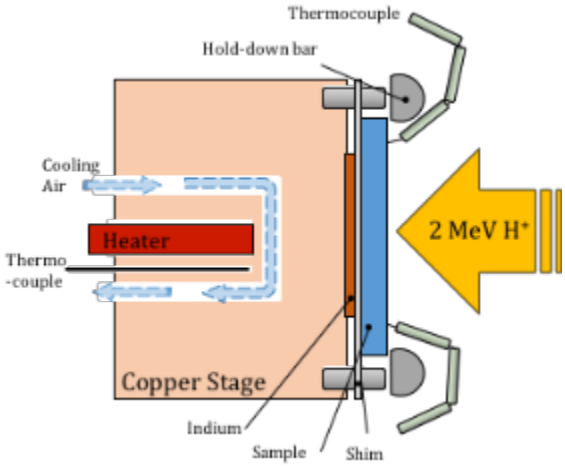

Figure 6. Schematic diagram of the cross-sectional view of the irradiation stage.

During the irradiation, infrared thermal images taken to monitor the temperature using a FLIR camera (A310 Series). Throughout the irradiation, the sample temperature was maintained at 360 ± 5 °C. Part of the temperature was due to the proton beam and the rest came from the heater. Before irradiation, the stage was first heated up to 360°C by the heater, to calibrate the emissivities for the infrared camera. Three ROIs (regions of interest) were selected in the irradiation area on each sample, upper, middle, and bottom, as shown in Figure 8. Once the proton beam hit the stage, the temperature increased sharply. The heater and the air cooling loop were adjusted based on the infra-red thermal image to achieve the irradiation temperature of 360°C. More detailed proton irradiation procedures have been represented elsewhere [15].

During the year 2014-2015, the 5 dpa proton irradiation experiments for four nickel-base alloys (Alloy 625, Alloy 625Plus, Alloy 725 and Alloy 625DA) were completed. During the year 2015-2016, the 5 dpa proton irradiation experiments for 690, alloy 310, 316L, 800 and T92 were completed.

Table 2. Irradiation experiments summary.

Alloys	Date	Final Dose
625	June 2015	5
625Plus	January 2015	4.15
725	April 2015	5
625DA	September 2015	5
316L	November 2015	5
706	December 2015	5
T92	February 2016	5
800	March 2016	5
Nickel-base	May 2016	5
690	June 2016	5
310	August 2016	5
C22	September 2016	5

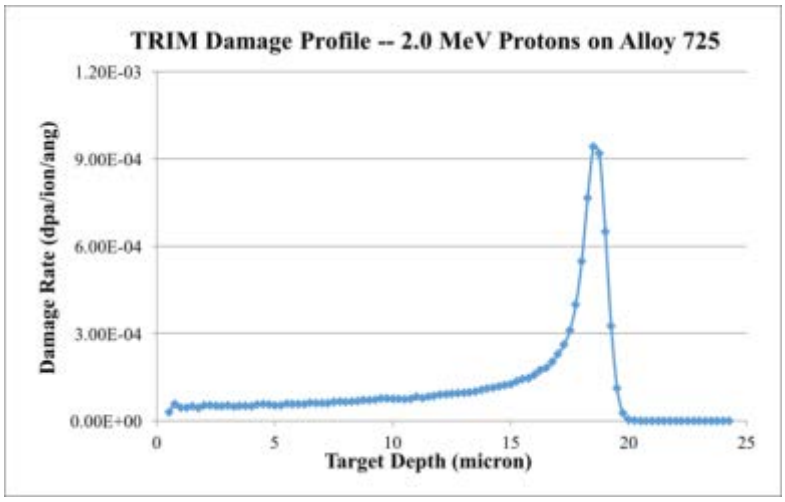

Figure 7. Damage profile in alloy 725 under 2 MeV proton irradiation.

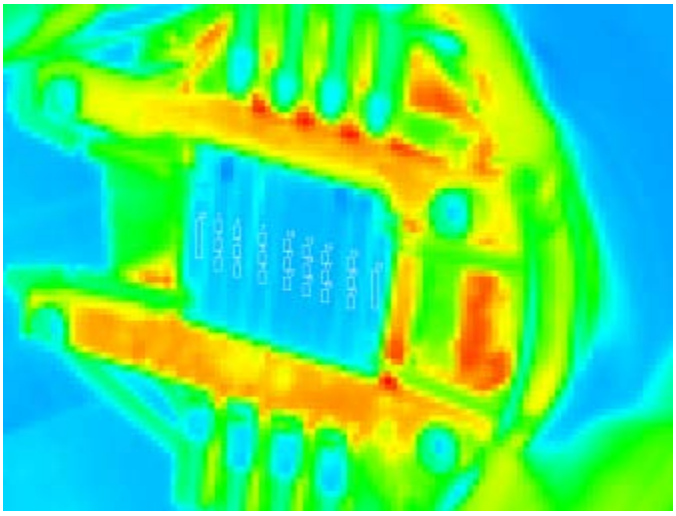

Figure 8. Infrared image of the irradiation stage (alloy 725).

2.4 Mechanical Properties Tests Conditions

2.4.1 Hardness measurement

Microhardness was measured using a Vickers Hardness indenter (MICROMET II) with a load of 25 g. The lower load (25 g) was chosen to confine the plastic zone ahead of the indenter tip to a depth within the proton irradiated range (~ 20μm) to ensure that the unirradiated region was not being sampled.

Samples used for hardness measurement were the same TEM samples used for proton irradiation. Thus, the polishing procedure was the same as described above. To evaluate the hardness changes due to irradiation, the hardness of the samples was measured at a load of 25 g before and after irradiation. Thirty indentations were made at each condition to ensure statistically relevant results. An average and standard deviation were determined for each condition.

2.4.2 Tensile test at room temperature

Tensile tests at room temperature were performed using an MTS machine (TR/50) and extensometer (MTS 634.12F-24) in the Irradiated Materials Testing Laboratory (IMTL) at the University of Michigan. The aim of the test was to obtain information about the mechanical properties of the alloys. The tensile test was conducted at a strain rate of 1×10^{-4} s^{-1} to failure at room temperature.

2.5 CERT System and Test Procedure

The Constant Extension Rate Tensile (CERT) tests were performed using the CERT I and CERT II systems in the High Temperature Corrosion Laboratory (HTCL) at the University of Michigan. CERT I and CERT II systems share the same design and are capable of straining four samples in parallel providing identical conditions within a given test, respectively. However, CERT I system is assigned to a BWR NWC environment while CERT II system is a PWR primary water environment.

The CERT experiments were conducted in a 4L autoclave that was connected to a flowing water loop fed from an external water column in which the addition of gas was made. The system also had a mechanical pump, a heater, a back pressure regulator (BPR), and conductivity and dissolved oxygen sensors on both the inlet and outlet of the autoclave. The water loop consisted of two water columns (the secondary column replenishes the primary column). Water flowed from the primary column, where gas can be bubbled to achieve the desired dissolved oxygen or hydrogen concentrations and where water conductivity and dissolved oxygen content was recorded before entering the high pressure pump. Before water entered the autoclave, it passed through a heat exchanger and a pre-heater to heat the water. Inside the autoclave, water was heated by resistive heaters outside of the autoclave that were controlled by a thermocouple in the autoclave (288°C for CERT I system and 320 °C for CERT II system). As water exited the autoclave, it passed through the heat exchanger, and then through a tube-in-tube chiller system. The BPR controlled the pressure inside the autoclave. The pressure of the water was reduced after passing through this regulator. The conductivity and dissolved oxygen (DO) concentration of the water were measured on the low pressure side of the loop. Subsequently, the water flowed through an ion exchange resin filter, a sub-micron filter, and back into the primary water column. For primary water chemistry, an ion exchange resin filter saturated with boron and lithium ions was installed in the loop so that the required concentrations of B/Li (e.g. 1000 ppm B and 2 ppm Li) were maintained while other impurities were removed. A schematic of the system (CERT II - PWR) is shown in Figure 9.

A stepper motor was used to strain the tensile samples at a constant displacement rate. It was controlled by digital outputs from the PC-monitoring system. The crosshead displacement was measured using a linear variable differential transducer (LVDT) with a resolution of 0.5 μm. Each of the pull rods were sealed at the feed-through into the autoclave with a self-energizing graphite seal with an internal spring that expanded under pressure. Each pull rod was connected to a Type 316L stainless steel sample

loading fixture. Electrical insulation was provided by zirconia washers located in the loading fixtures. After the test specimens were loaded, the autoclave body was sealed to the autoclave head.

CERT experiments were conducted at a strain rate of 1 x 10^{-7} s^{-1} in either simulated BWR-NWC (288°C, 1500 psi, 2000 ppb dissolved oxygen) or PWR primary water environment (320°C, 2000 psi, 35cc/kg dissolved hydrogen, 1000 ppm [B] and 2 ppm [Li]) environments to about 4 % plastic strain. The conductivity, oxygen content, hydrogen content, and B and Li concentrations were chosen to be representative of both reactors cores. The specific conditions are listed in Table 3.

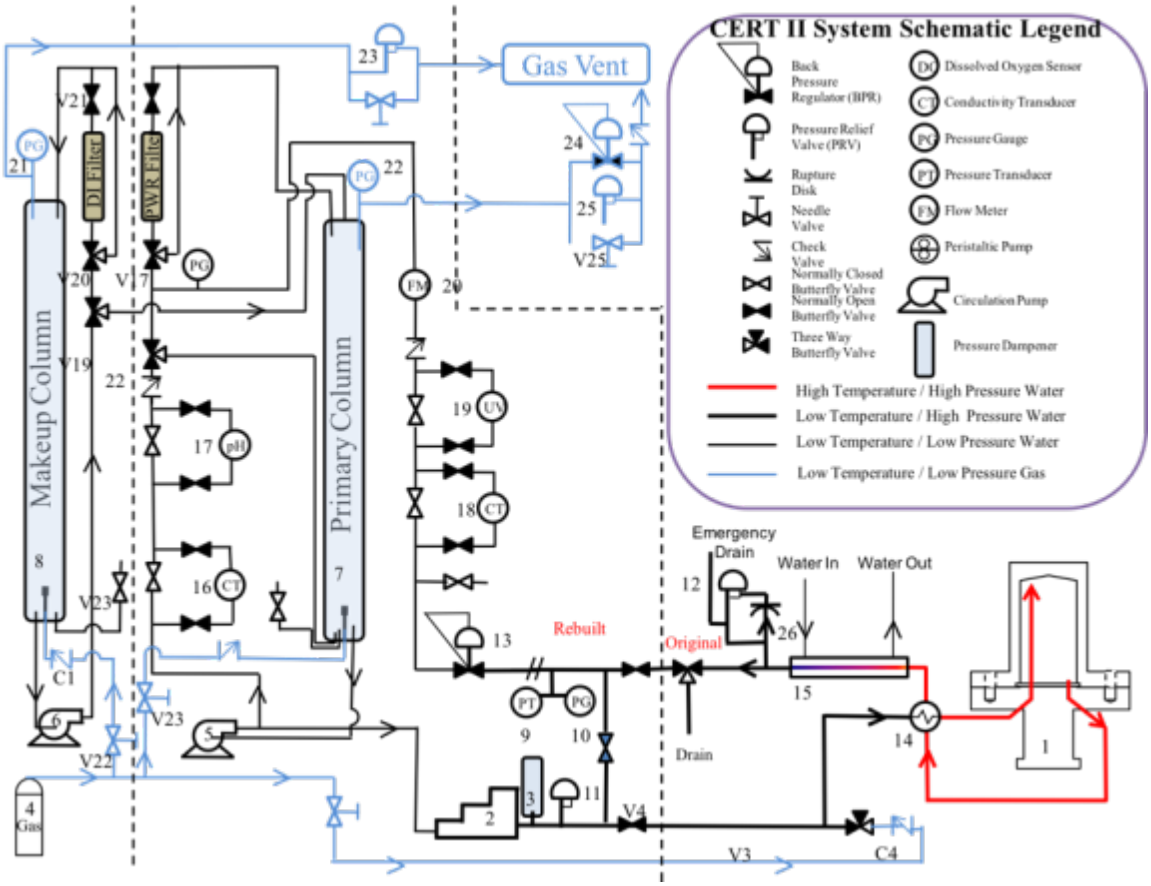

Figure 9. A schematic design of CERT (CERT II - PWR) test system.

2.6 Characterization of Cracking Susceptibility

After the CERT test, each tensile sample was characterized in a scanning electron microscope (SEM) model JEOL JSM-6480, to determine the surface morphology and cracking susceptibility:

- Lower magnification images were taken throughout the tensile sample surfaces to get the general information on the sample.
- Higher magnification images were taken on some specific features, such as on the cracks or precipitates, etc…
- Intermediate magnification images were taken on three random areas in both irradiated and unirradiated regions for statistical counting of the cracking behavior.

Based on the information generated, a comparison of cracking susceptibility among the different alloys can be measured.

Table 3. Conditions of CERT test for simulated BWR (NWC) and PWR environments.

Parameter	BWR (NWC)	PWR
Temperature (°C)	288	320
Pressure (psi)	1500	2000
Inlet Conductivity (μS/cm)	< 0.1	20-35
Outlet Conductivity (μS/cm)	< 0.1	20-35
O_2 Concentration (ppb)	2000	< 5
H_2 Concentration (cc/kg)	-	35
[B] (ppm)	-	900-1100
[Li] (ppm)	-	2-3
pH at 25°C	7.0	6 – 6.7

3. RESULTS

3.1 Irradiation Experiments

During each irradiation, various experimental parameters were recorded. The following results were from the proton irradiation of alloy 725 to a dose of 5 dpa and were used as an illustration of the recorded data. Pressure of the entire beam line is plotted in Figure 10, and beam current is shown in Figure 11. Temperature history diagrams of each sample are plotted in Figure 12.

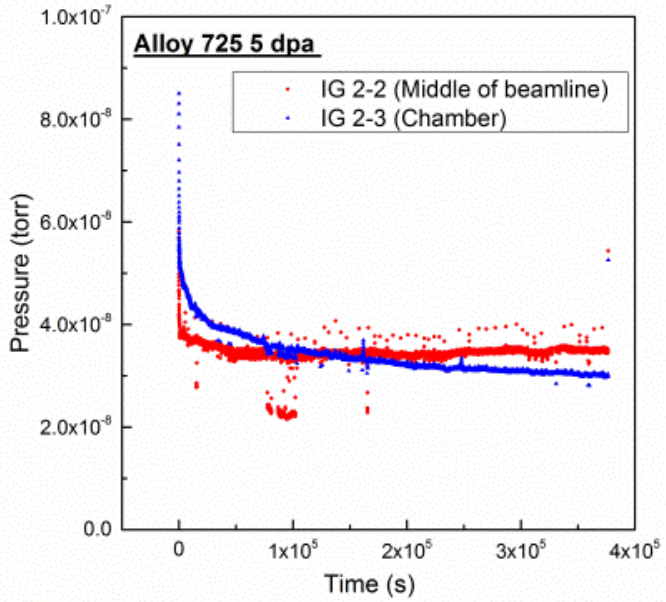

Figure 10. Pressure of the beam line during the Irradiation of alloy 725 to a dose of 5 dpa.

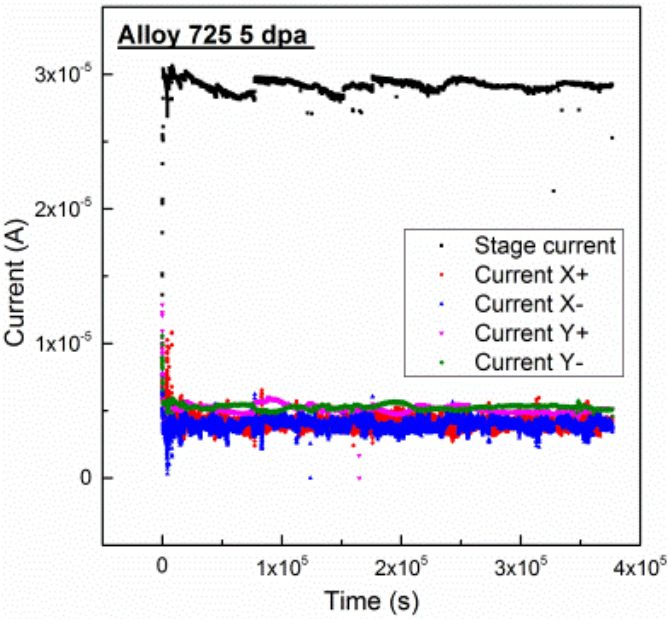

Figure 11. Current of the irradiation of alloy 725 to a dose of 5 dpa.

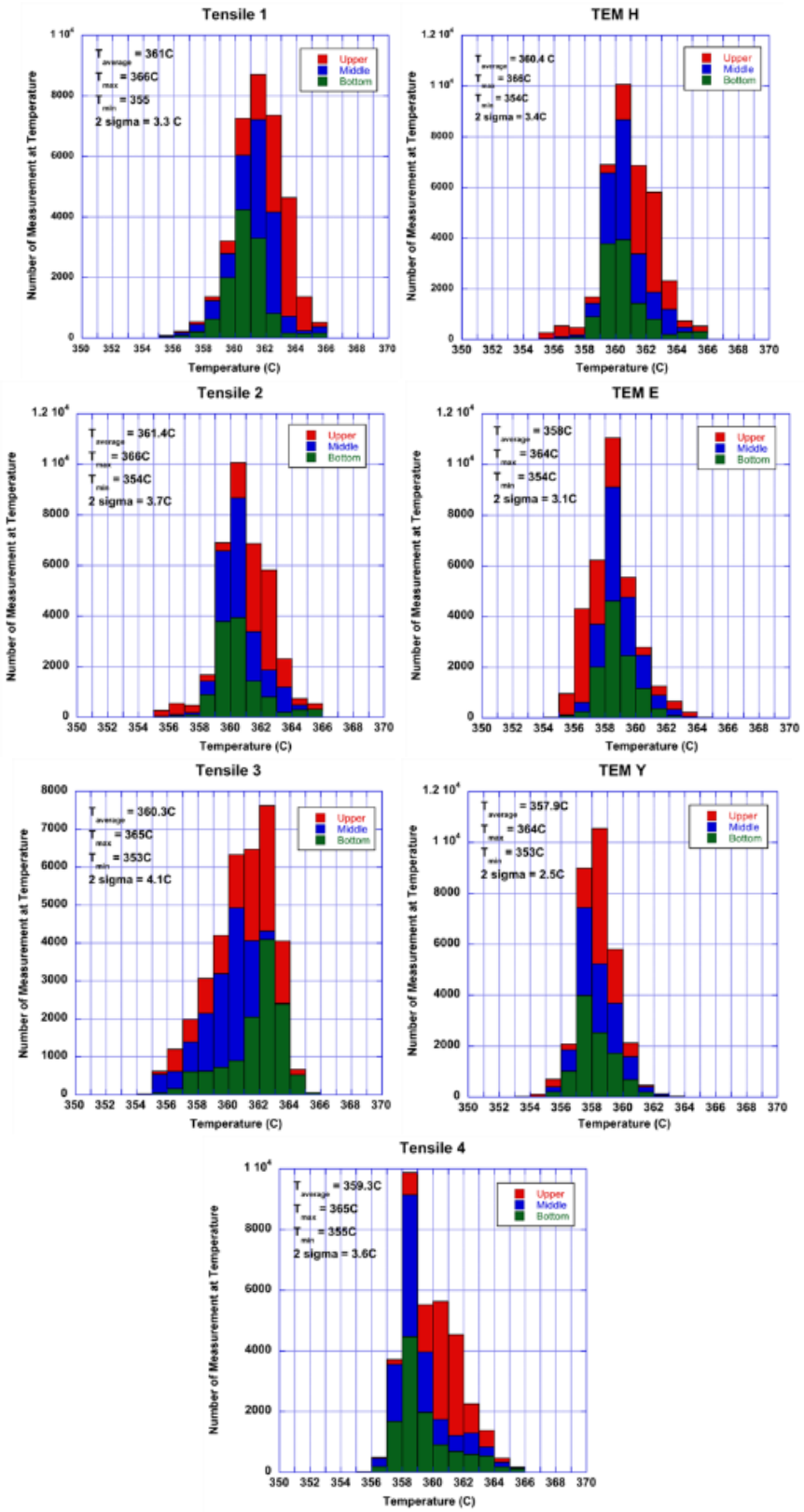

Figure 12. Temperature histroy diagrams of alloy 725 during the irradaition to a dose of 5 dpa.

The pressure of the chamber where the stage was located was between 10^{-7} and 10^{-8} torr. Under this high vacuum, no oxide was formed on the surface of the sample during the irradiation. The total current was around 50 μA, which was the maximum stable beam current that was achieved by the accelerator. About two-thirds of the beam, about 30 – 35 μA, was on the stage with the balance on the slits. This ensured that the samples were fully irradiated during the raster-scanning process. The temperature histogram showed the temperature distribution of three different positions located in the irradiation area of each sample. Generally, it follows a normal distribution, and the three positions: upper, middle, and bottom, were overlapped with each other. The average temperature for each sample was around 360 °C, and the standard derivation valve is less than 4.1 °C. Monitoring all the irradiation parameters ensured that the proton irradiation was well controlled.

The beta counting was conducted for each sample after irradiation to confirm that the samples were irradiated uniformly. The bar diagram of beta counting of the irradiation of alloy 725 to a dose of 5 dpa is shown in Figure 13. Guide samples (in grey) were not fully irradiated, thus they had lower beta counts. Four tensile and three TEM samples (in red) in the middle of the stage had very close beta counts, indicating that they were fully and uniformly irradiated.

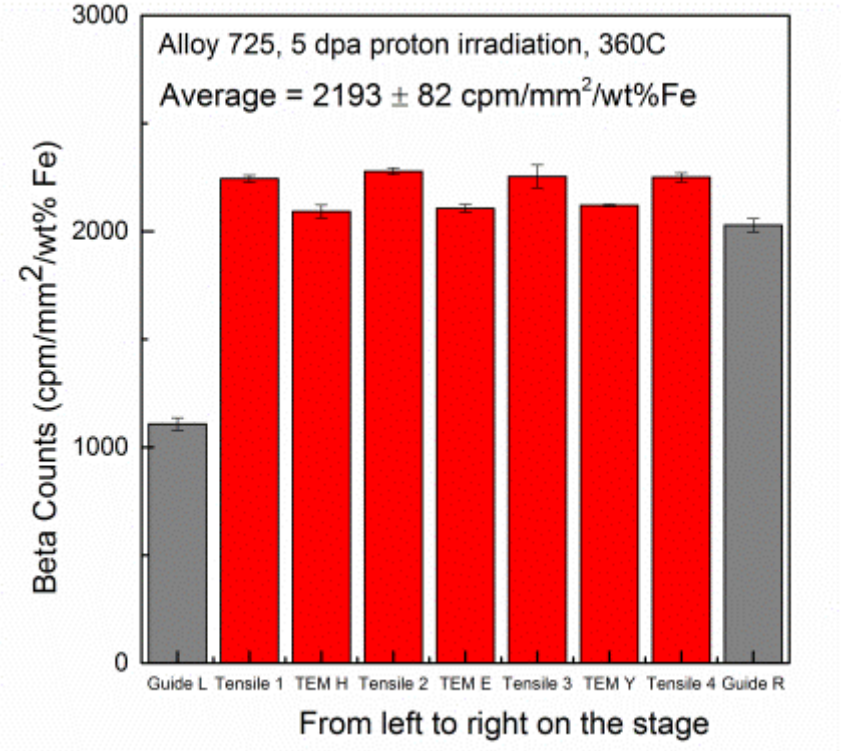

Figure 13. Bar diagram of beta counting of each sample after irradiation of alloy 725.

3.2 Microstructure Pre-characterization

The pre-characterization of microstructure involves the grain size distribution, grain boundary character, and precipitates identification. The grain boundary chemistry characterization will be reported in the radiation induced segregation session.

3.2.1 Grain structure and GB characterization

The average grain sizes of these alloys were listed in Table 4. Alloy 625Plus has the largest average grain size while the average grain size of Grade 92 is the smallest. In the nickel base alloy, alloy 625DA shows the smallest average grain size about 10 μm. The grain boundary characters of all the alloys were listed in Table 5. The follow will be some examples from the nickel base alloy 625 family.

Table 4. The average grain size of as-received materials

Alloy ID	Grain size (μm)	# of grain involved
625	40±17	221
625Plus	120±87	223
625DA	12±7	365
725	60±32	366
316	81±45	90
310	TBD	TBD
690	86±56	120
800	62±38	110
T92	0.56±0.54	1080

Table 5. Grain boundary character based on EBSD measurements

ID	LAGB		HAGB		Special GB		Random High angle		Area
	L(μm)	Fraction, %	L(μm)	Fraction,%	L(Σ3+ Σ9)	Fraction,%	L (μm)	Fraction,%	(μm^2)
625	565.8	2.1	26,000	97.9	16,808+1,228	67.9	7,964	30	90,530
625Plus	743	1.1	67,800	98.9	50,117+2,369	76.6	15,314	22.3	1,012,842
625DA	229	2.8	7,990	97.2	4,021+209	51.5	3,760	45.7	13,457
725	506	2	24,900	98	16,414+512	66.6	7,974	31.4	235,292
316L	4,360	10.2	38,300	89.8	17,300+621	42.2	20,379	47.6	491,916
310	867	4.5	18,700	95.5	8,830+197	46.2	9.673	49.3	50,388
690	2,352	8.6	25,000	91.4	13,100+432	49.3	11,468	42.1	276,049
800	945.1	2.5	36,400	97.5	22,500+1,760	65.1	12,140	32.4	389,518
T92	3,970	40.1	5,920	59.9	N/A	N/A	5, 920	59.9	46,737

LAGB: low angle grain boundary, grain boundaries lower than 15°
HAGB: high angle grain boundary, grain boundaries larger than 15°
N/A: not applicable

A general feature of these nickel-base alloys is large grain size with (Nb,Ti)(C,N) stringers along the extrusion direction as shown in Figure 14. More particles are observed in alloys 625 and 625 DA compared to that in alloys 625Plus and 725. Between alloy 625 and alloy 625DA, alloy 625DA has the higher stringer content. NbC is formed during the solidification and is hard to remove by the subsequent heat treatments. Using alloy 725 as an example, two types of primary particles were observed as shown in Figure 15a, both of which can be written in the formula (Nb,Ti)(C,N) vs. NbC. The large particles were rich in Ti and N and appeared as stringers along the extrusion direction. The average particle size was around ~5.5 μm. The chemical composition (in wt.%) of a representative particle was 3.63 C, 14.37 N, 0.89Al, 11.17 Nb, 69.0 Ti, 0.93Cr as shown in Figure 15c. The smaller particles were dominated by Nb and C elements, and had an average size of ~290 nm. The EDX analysis shown in Figure 15d indicated a chemical composition (in wt.%) as follows: 10.7 C, 3.28 Al, 20.14 Nb, 7.78 Mo, 4.65 Ti, 14.31 Cr, 0.24 Mn, 5.22 Fe, 33.67 Ni. Due to the small size of the particle compared to the interaction volume, the matrix elements were inevitably collected. EDX measurements were taken at a minimum of five points on

each of these particles. Specially, these NbC particles are typically lined up and situated at the ghost boundaries as shown in Figure 15a. The ghost boundary is the position of deformed previous boundaries of casting grains. Later, the recrystallization eliminated the previous boundaries of casting grains while the precipitates remained. However, not all the nickel-base alloys investigated here showed ghost boundaries.

The average grain size was measured by a linear interception method with at least 200 grains involved for each alloy. The statistical results of grain size distribution are listed in Figure 16. Alloy 625Plus shows the largest average grain size of around ~120μm. Alloy 625DA showed the smallest average grain size of around ~12 μm. These nickel-base alloys possess high length fraction of annealing twin boundaries. The twin boundaries (TB) are highlighted in red while the regular high angle grain boundaries are in black as shown in Figure 17. The regular high angle grain boundaries constituted a length fraction of 30% in alloy 625, 22% in alloy 625Plus, 46% in alloy 625DA, and 32% in alloy 725. It was easy to distinguish these random high angle grain boundaries from twin boundaries, as the latter typically appeared as straight lines in the TEM. The EBSD results showed that the length fraction of TB, mainly Σ3 boundary, was above 50% of the total length of GB. A high fraction of these kinds of coincidence site lattice (CSL) boundaries can enhance the corrosion resistance of these alloys in practical applications [16]. All the statistical data are listed in Table 5, which is related to the grain boundary information. It was noticed that the length fraction of low angle boundaries was less than 3% for all alloys.

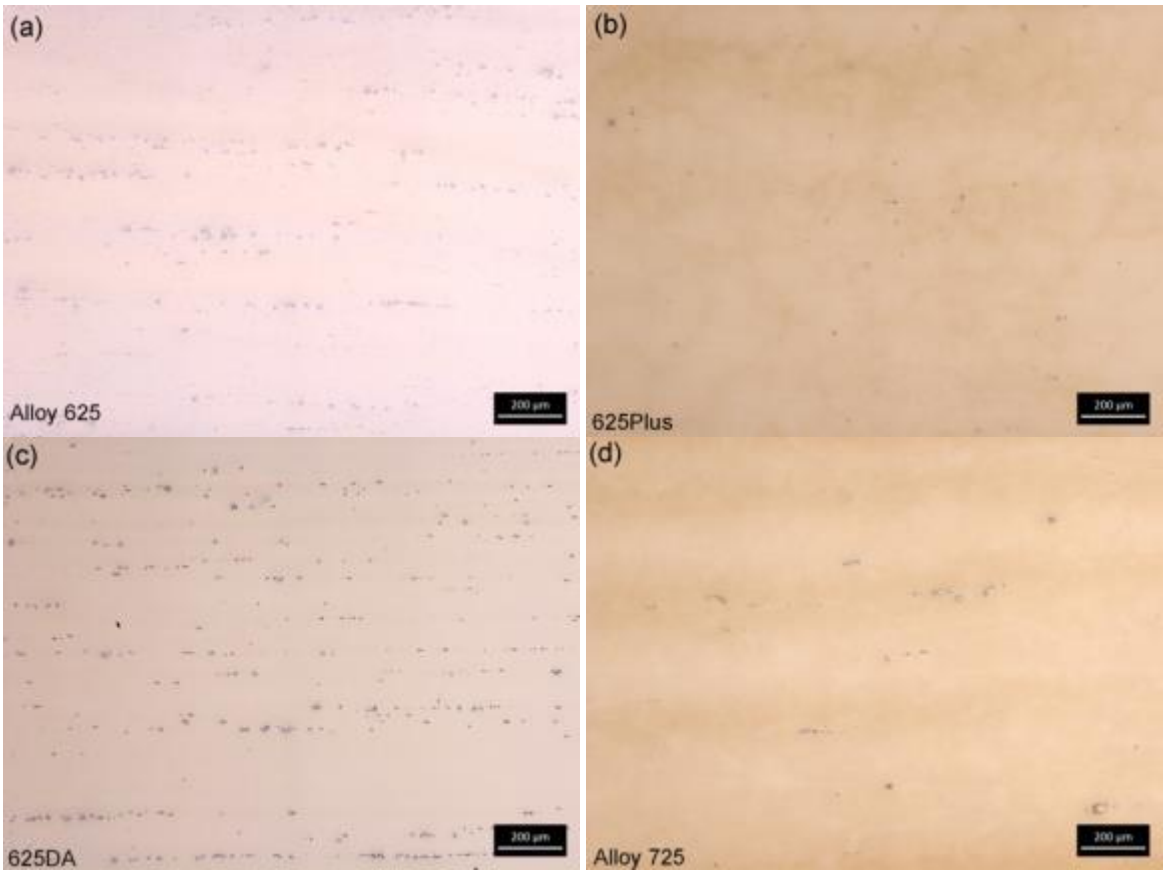

Figure 14. Optical images of (a) alloy 625 (b) alloy 625Plus (c) alloy 625DA and (d) alloy 725 show the formation of stringers. More particles are observed in alloy 625 and alloy 625DA than in alloy 625Plus and alloy 725.

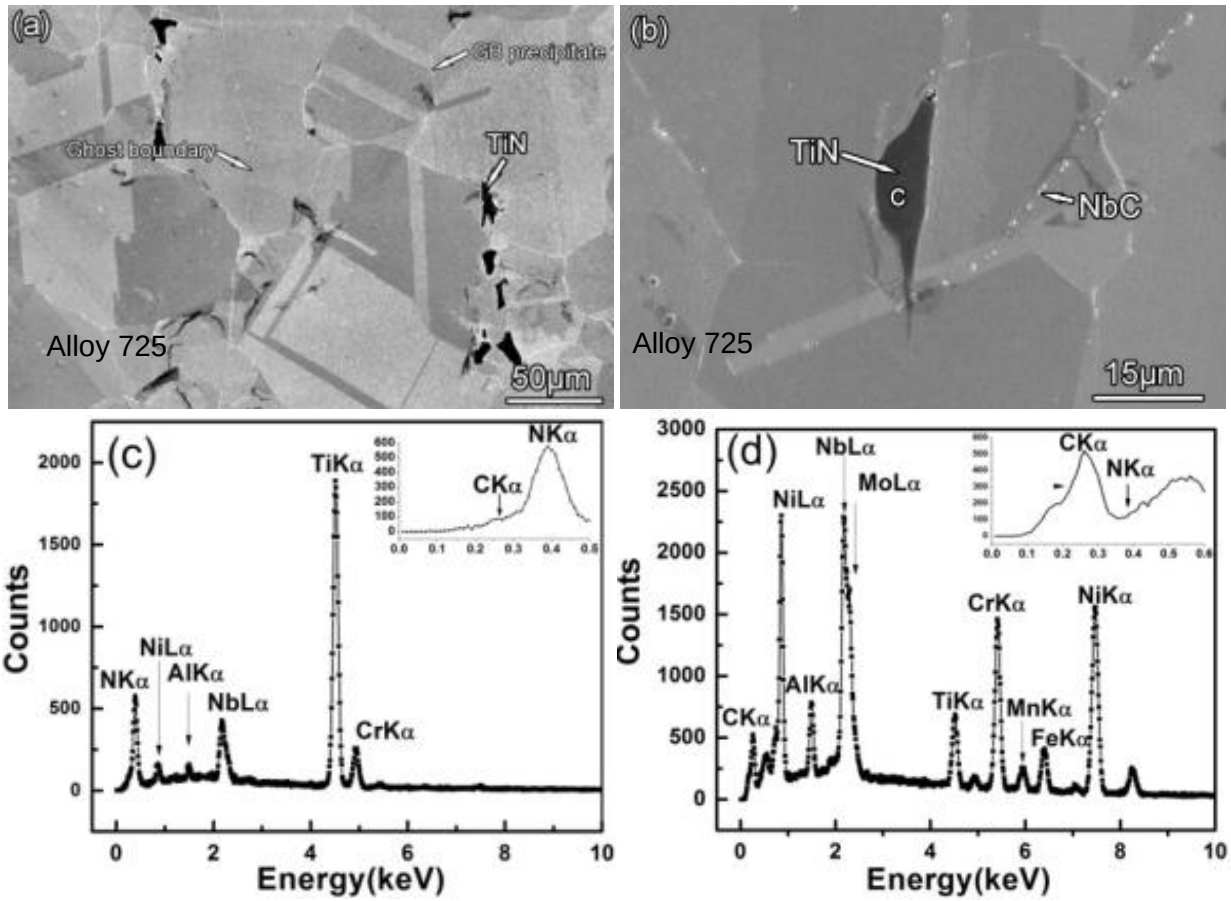

Figure 15. Secondary electron image and EDX of alloy 725. (a) Secondary electron image shows the basic structure of alloy 725. (b) The large black particles are commonly Ti, N riched (Ti,Nb)(C,N) as revealed by (c). (d) The EDX of a small particle similar to those marked as NbC in (b) shows the enrichment of Nb and C elements. The inserted EDX spectrumwith an energy range from 0~0.6keV shows that the relative amounts of N and C are different in these particles. An unidentified grain boundary precipitates (possible μ phase) are noted as the white line along the GB.

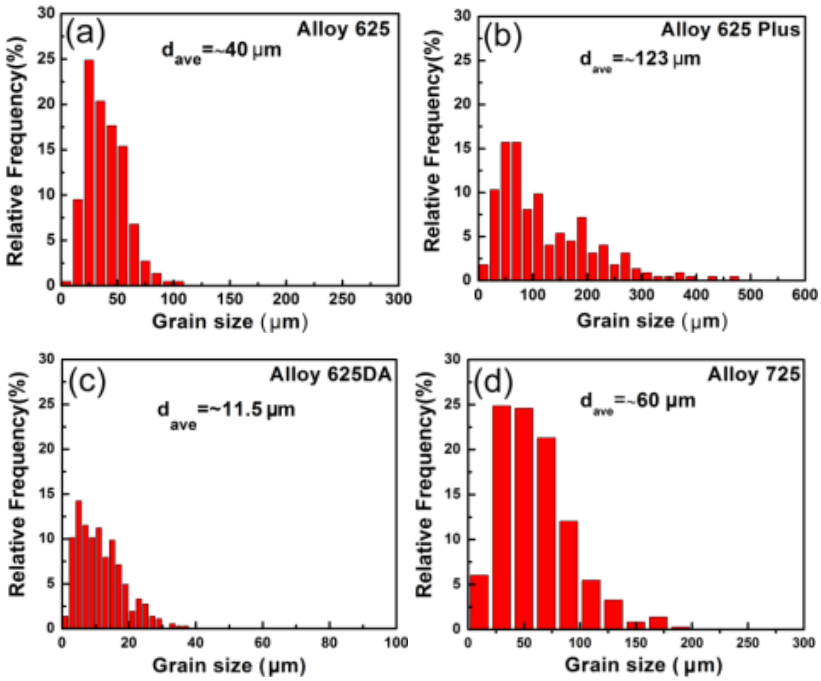

Figrue 16. Grain size distributions of alloys investigated (a) alloy 625, (b) alloy 625Plus, (c) alloy 625DA, (d) alloy 725. 625DA shows the smallest average grain size while alloy 625Plus exhibit the largest grain size around 120μm.

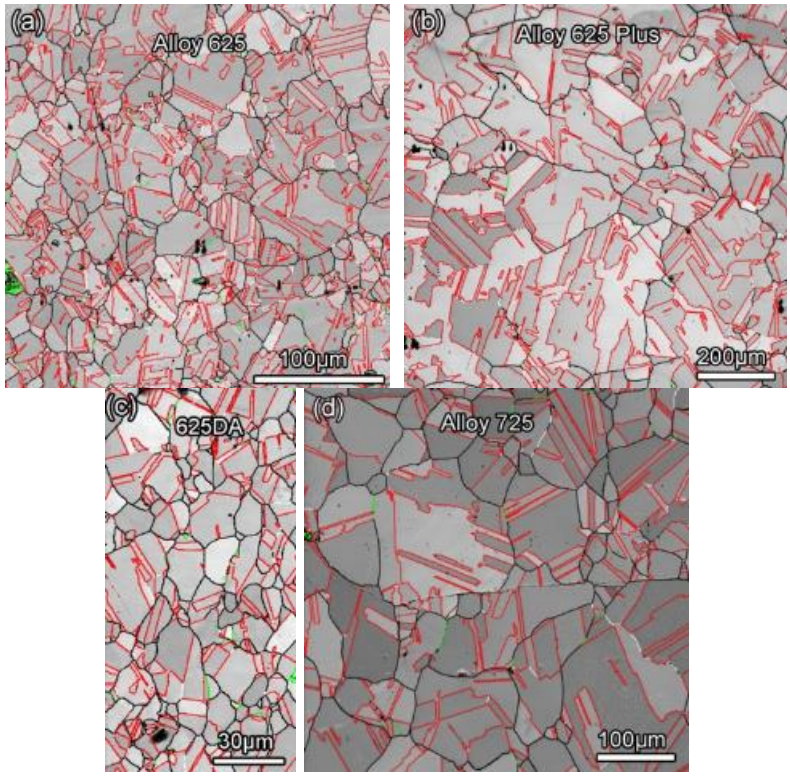

Figure 17. EBSD image quality map for various nickel base alloys (a) alloy 625 (b) alloy 625Plus (c) alloy 625DA and (d) alloy 725. The high and low angle boundaries are shown as black and light green, respectively. Σ3 and Σ9 boundaries are shown as red and white' respectively.

3.2.2 Twin boundaries

Twin boundary (TB) possesses a very high length fraction in these austenitic base alloys. It is quite important to understand its structure. Figure 18 shows the fine structure within a grain of alloy 625. Three variants of twins were observed in the grain. They are marked as T1, T2 and T3, respectively. They all belong to the {111} <112> type twins, where the twin plane {111} is the close packed plane and <112> is twin direction. In those three variants, T1 and T2 are edge-on twins with the matrix, where T3 is an inclined twin. The two edge-on twins were confirmed by the diffraction spots where a mirror-type diffraction pattern was developed. For the inclined twin, no mirror-type diffraction pattern was observed as shown in Figure 18f. The twin relationship was determined based on the crystallographic orientation relationship between the twin and the matrix.

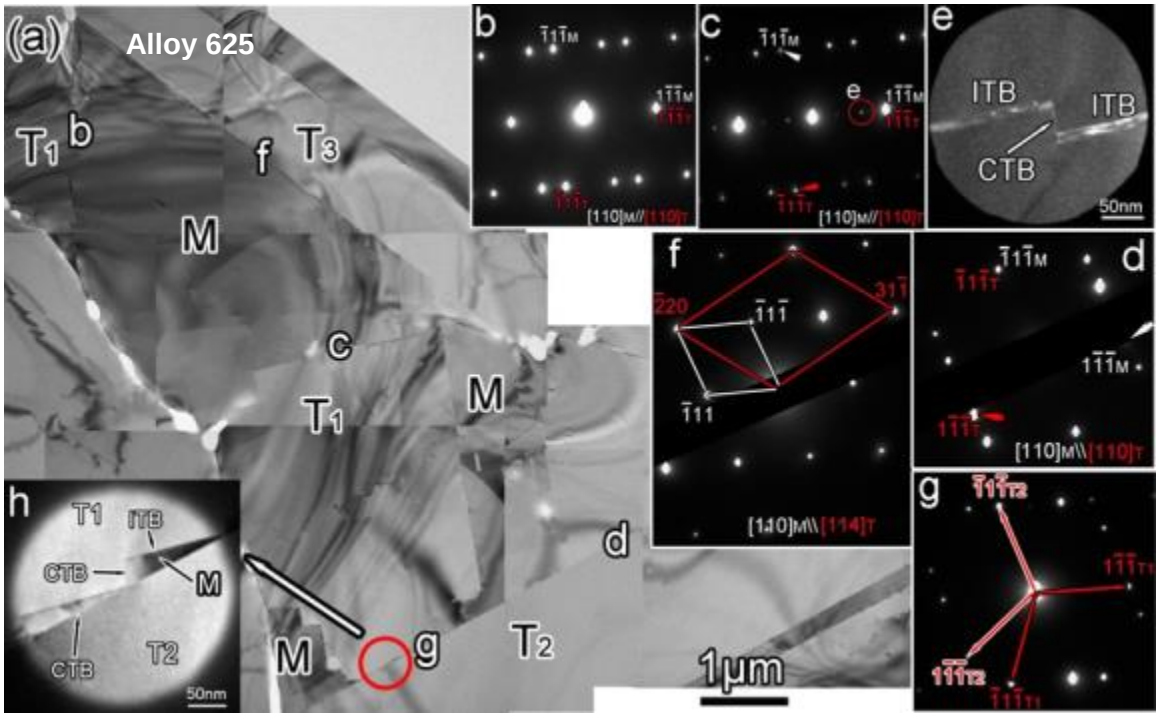

Figure 18. Detailed twin structure within a single grain in alloy 625. Three variants of twins are observed. They all belong to the {111}<112> type. T1 and T2 are edge on twins with the matrix. T3 are inclined twin with the matrix.

3.2.3 Intragranular precipitate characterization

Except for alloy 625, the other alloys of this family were all precipitation hardened. A general feature of these alloys is that substantial amounts of precipitates were observed within the matrix, with a density on the order of $10^{22}/m^3$ as shown in Figure 19. A simple method of identifying the γ′ phase based on the co-precipitation was introduced by Cozar and Pineau [17]. By using this method, no γ′ phase was observed, suggesting that the amount of γ′ phase was negligible. The inserted selected area diffraction pattern (SADP) corresponded well to the γ′′ phase, which is an ordered body-centered-tetragonal (bct) DO22 structure with lattice parameters $a_{\gamma''}=b_{\gamma''}\cong a_{\gamma}$, and $c_{\gamma''}\cong 2a_{\gamma}$. The established orientation relationship [17] between γ′′ and the matrix is (001)γ′′//{001}γ, and [100] γ′′//<100>γ. Three variants of γ′′ phase were precipitated due to the symmetry of the matrix as shown in Figure 19b_i-d_i. The [001]γ zone axis is

explored because three variants can be easily distinguished [18]. Also, images from this particular zone axis can provide information about both diameter and thickness of the γ'' phase. Most of the observations in this study were performed in this direction as the diffraction spots of three variants were distinguished without overlap with the matrix. The precipitates are disk-shaped with short dimension along the c-axis. The largest average diameter was around ~ 18 nm and the average thickness was about ~8 nm in alloy 725. The precipitates in Alloy 625Plus and 625DA show similar size of ~ 12 nm in diameter and ~ 6 nm in thicknesses. The statistical results are given in Figure 20 and were based on measurements of about 400 particles for each case. It should be noted that the γ'' precipitates were distributed inhomogeneously in alloy 625DA, where a significant bias in the variants was observed. This bias in the variants was always associated with dislocations.

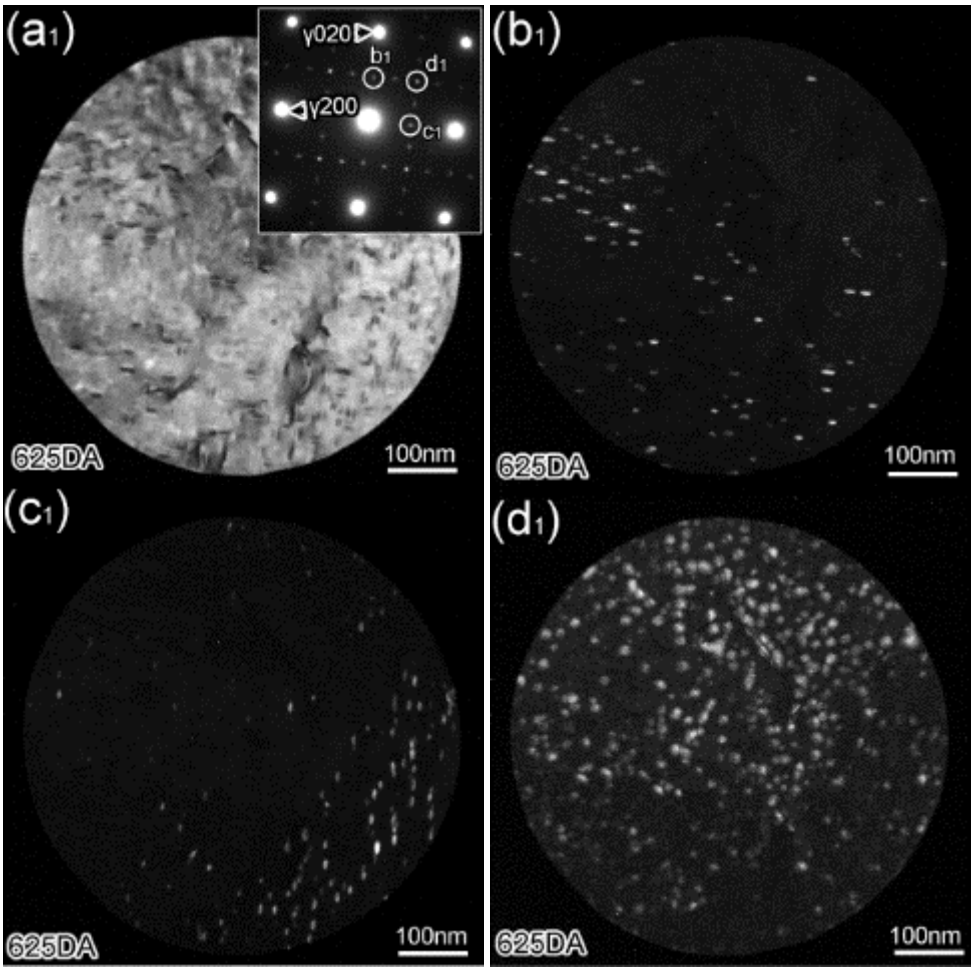

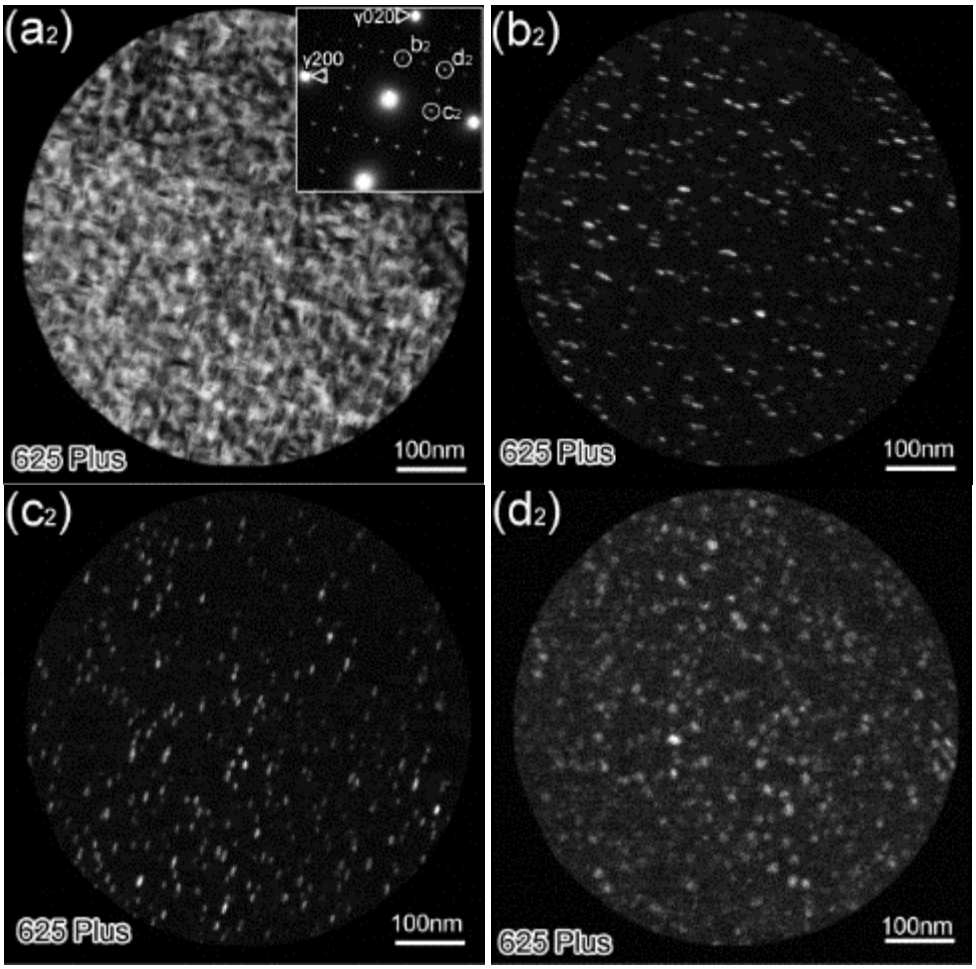
(a2)
γ020
γ200
b2
d2
c2
625 Plus
100nm
(b2)
625 Plus
100nm
(c2)
625 Plus
100nm
(d2)
625 Plus
100nm

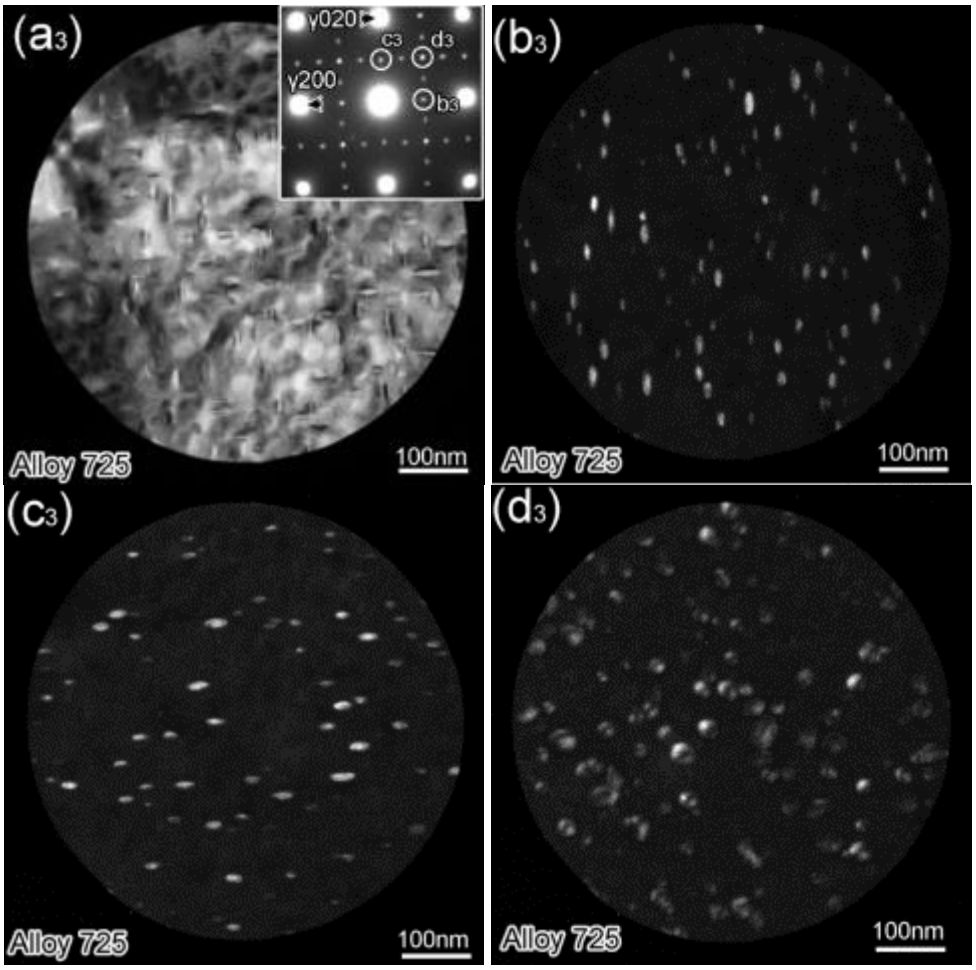

Figrue 19. Bright field (BF) and dark field (DF) TEM image of γ'' precipitates in (a1-d1) alloy 625DA (a2-d2) alloy 625Plus (a3-d3) alloy 725. (a1) BF image shows that massive precipitates are homogeneously distributed within the grain. (b1-d1) DF TEM images show all three variants of γ'' precipitate respectively using the spots circled in selected area diffraction pattern (SADP) inserted in (a1). A biased distribution between variants was observed in alloy 625DA.

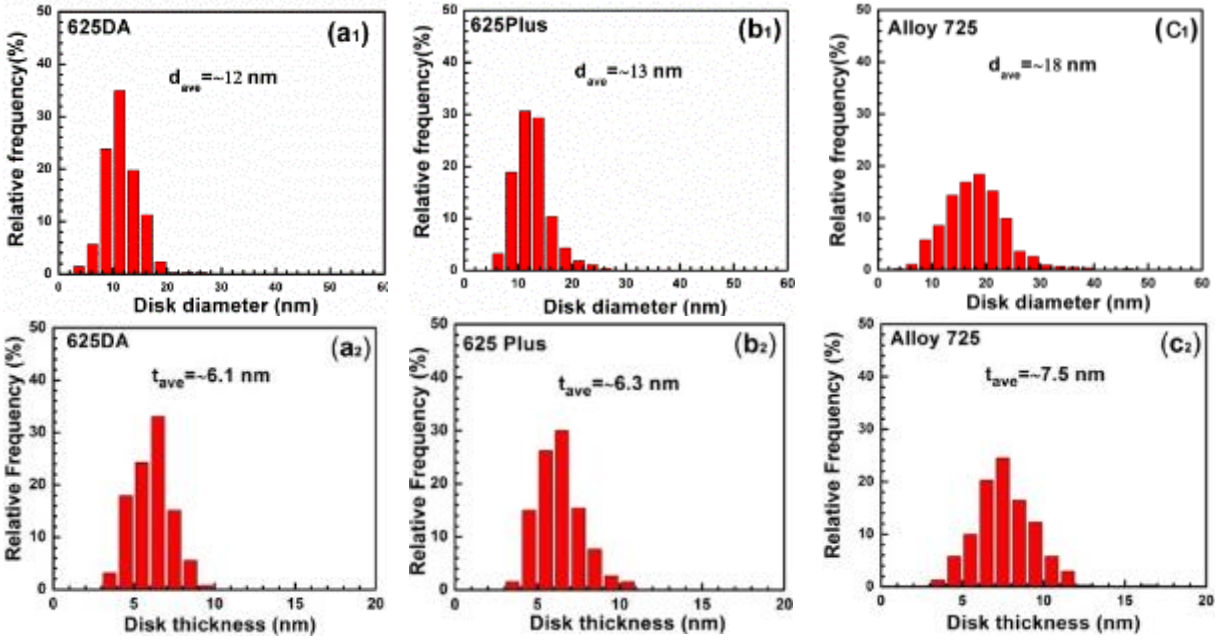

Figure 20 Size distribution of γ" phase along disk diameter (a1) 625DA and (b1) 625Plus and (c1) alloy 725, along disk thickness (a2) 625DA and (b2) 625Plus and (c2) alloy 725. The precipitate in alloy 725 shows a coarser size in both diameter and thickness dimensions. The precipitate in alloy 625DA and alloy 625Plus are within the error bar.

3.2.4 Microstructures of other alloys

The as-received microstructures of austenitic alloys 316L, 310, 800, and 690 were composed of clean grain structure with some grain boundary carbides shown in Figure 21. The microstructure of T92 was different which can be generally described as a hierarchal structure. From the experience of low carbon alloys, lath martensite usually exhibited as packets and blocks [19, 20]. By combination of the morphology and crystallography, Morito *at al.* proposed a hierarchal microstructure for the configuration of these lath martensites [21, 22]. The prior austenite grain boundary (PAGB) is the highest level of microstructure in these alloys.

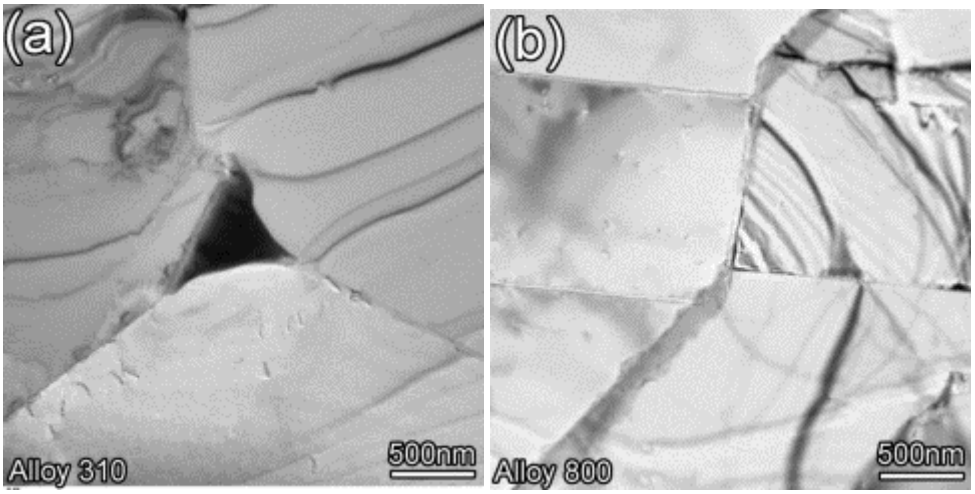

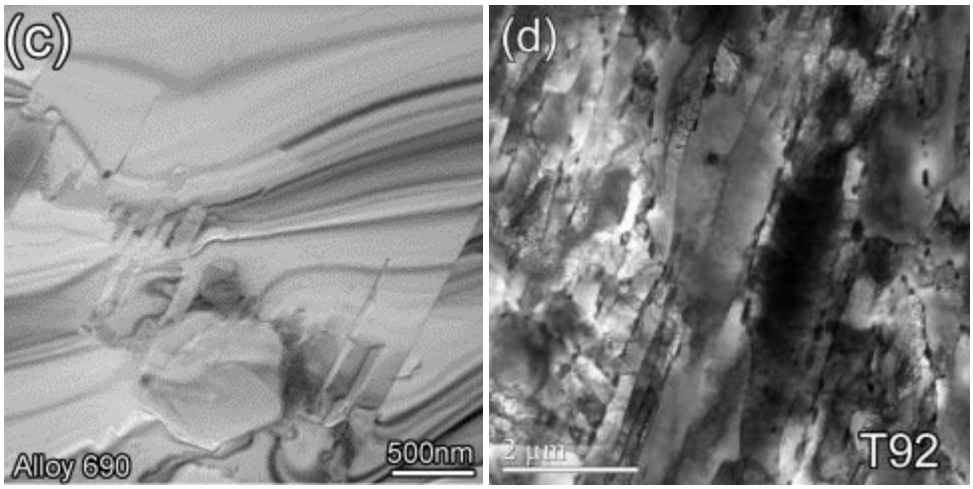

Figure 21. As received microstrucutre of (a) alloy 310 (b)alloy 800(c) alloy 690 and (d) alloy T92

3.2.5 Precipitate free zones around primary precipitates

Figure 22 shows the precipitate-free zone (PFZ) around a primary particle in alloy 725. The extra diffraction spots derived from the primary particle correspond well to a (002) plane d-spacing of NbC, which is a FCC structure with the lattice parameter of 0.447 nm. No orientation relationship can be identified between these NbC particles and matrix due to the incoherent interface. A potential reason for this observation is that after the nucleation of the NbC precipitate, the orientation of the surrounding matrix was changed due to the recrystallization process, thus the orientation relationship between the matrix and particles cannot be maintained. The PFZ became apparent in DF images (Figure 22.b) of all the three variants of γ'' precipitate. The width of the PFZ ranges from 50~90 nm. A dislocation line was observed in the STEM image in Figure 22.c. An EDX line scan (Figure 22.d) confirmed that the particle had a composition close to that of (Nb,Ti)C, which was similar to particles situated at ghost boundaries.

Interestingly, these kinds of PFZs showed strong variant dependence as shown in Figure 23a-c. Even in a single variant scenario (for example, in Figure 23a), the PFZ varied with the shape of precipitates. The smallest dimension of PFZ occurred at a corner of the primary particle, with a size of ~60 nm. Meanwhile, the largest dimension occurred at a facet of the primary particle, with a size of ~450 nm. For the second variant, the shape of the PFZ is similar to that of the first variant as shown with a 90 degree rotation in Figure 23b. The third variant was less affected by the shape of the primary particles and a similar width of the PFZ was observed all around the periphery of the primary particle. Enhanced precipitation of the third variant was observed in the overlapped region of the PFZs related to variants one and two.

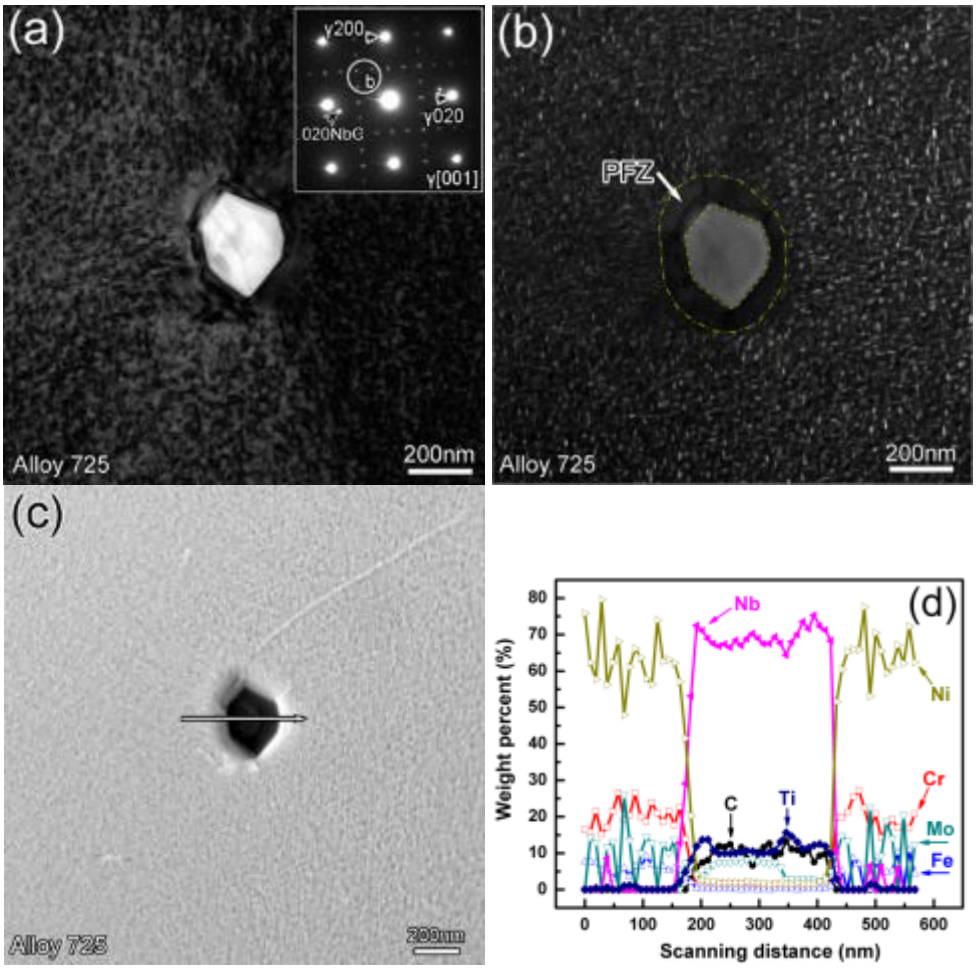

Figure 22. PFZ in the vicinity of a primary particle in alloy 725. (a) BF TEM image shows inhomogeneous distribution of γ'' precipitate around a primary particle. (b) PFZ was obvious in DF TEM image. (c) STEM image and (d) corresponding line scanning reveal that primary particle is Nb enriched carbides.

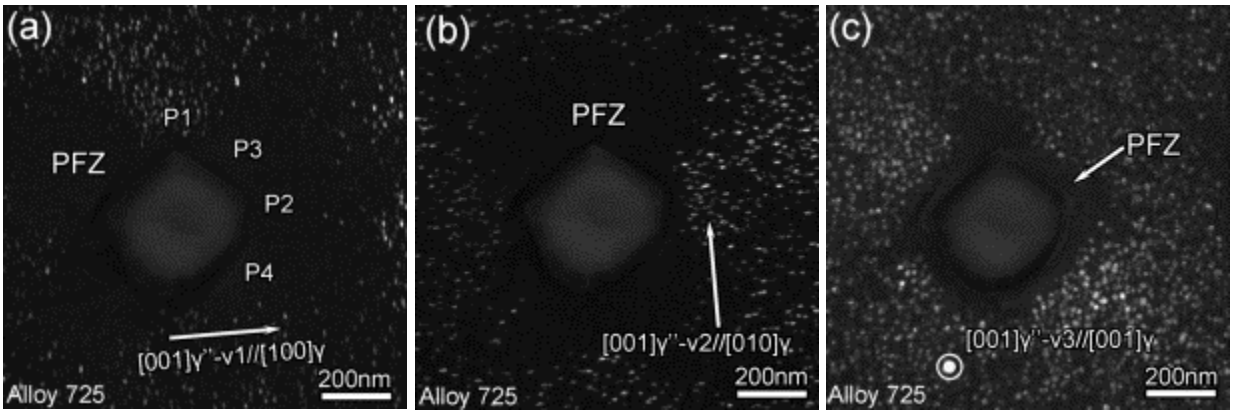

Figure 23. Variant dependent PFZ around a primary particle (a-c) in alloy 725. The PFZ shows variant dependence and was significantly influenced by the particle shape.

To verify that the variant dependent PFZ was not limited to [001]γ direction, [-1-11]γ zone axis was investigated near another primary particle as shown in Figure 24, which was another direction with three distinguishable variants. The orientation relationship between the matrix and γ'' turns out to be (204)γ''//{202}γ, and [221] γ''//<111>γ , which was consistent with (001)γ''//{001}γ, and [100] γ''//<100>γ if the lattice parameters $c_{\gamma''} \cong 2a_{\gamma}$ were taken into consideration. Again, a variant-dependent PFZ was observed around NbC. Aligned γ'' precipitates were also noted following a crystallography direction close to [110] in Figure 24b and c. These precipitates are likely to be associated with dislocations at earlier stages. Table 6 summarizes the general microstructural features of nickel-base alloys. No texture was observed for any of the samples involved.

Table 6. Microstructure feature of as-received nickel based alloys

	Microstructure Feature									
	Grain structure					Precipitation				
Materials	Grain size (μm)	#	TB length fraction (%)	Area counted (μm^2)	Texture	γ'' phase diameter (nm)	#	γ'' phase thickness (nm)	#	Density ($10^{22}/m^3$)
625	40±17	221	67.9	90,530	N	N	N	N	N	N
625Plus	120±87	223	76.6	1,012,842	N	13±3.3	928	6.3±1.4	260	4.5±3.5
625DA	12±7	365	51.5	13,457	N	12±3.1	640	6.1±1.2	251	1.7
725	60±32	366	66.6	235,292	N	18±6.0	723	7.5±1.8	310	2.9±1.2

N = not observed, # = number counted

3.3 Microstructure Characterization of Irradiated Alloys

The microstructure of irradiated alloy generally includes dislocation loops, irradiation induced or enhanced precipitates, voids, and radiation induced segregation. Table 7 summarizes the irradiation induced feature observed in the alloys examined. All the irradiation microstructure will be introduced in this part.

Table 7. Microstructure features characterized in the irradiated materials.

Alloy ID	Microstructure features of irradiated materials			
	Irradiation induced precipitates	Loops	Voids	RIS
625	LRO	Y	N	Y
625Plus	LRO	Y	N	
625DA	LRO	Y	N	
725	LRO	Y	N	
690	LRO+γ'	Y	N	
316L	ND	Y	Y	
310	γ'	TBD	Y	
800	γ'	TBD	N	

LRO: long range order phase, Ni_2Cr type precipitate. ND: nothing detected. TBD: to be determined. N: not existing. Y: existing.

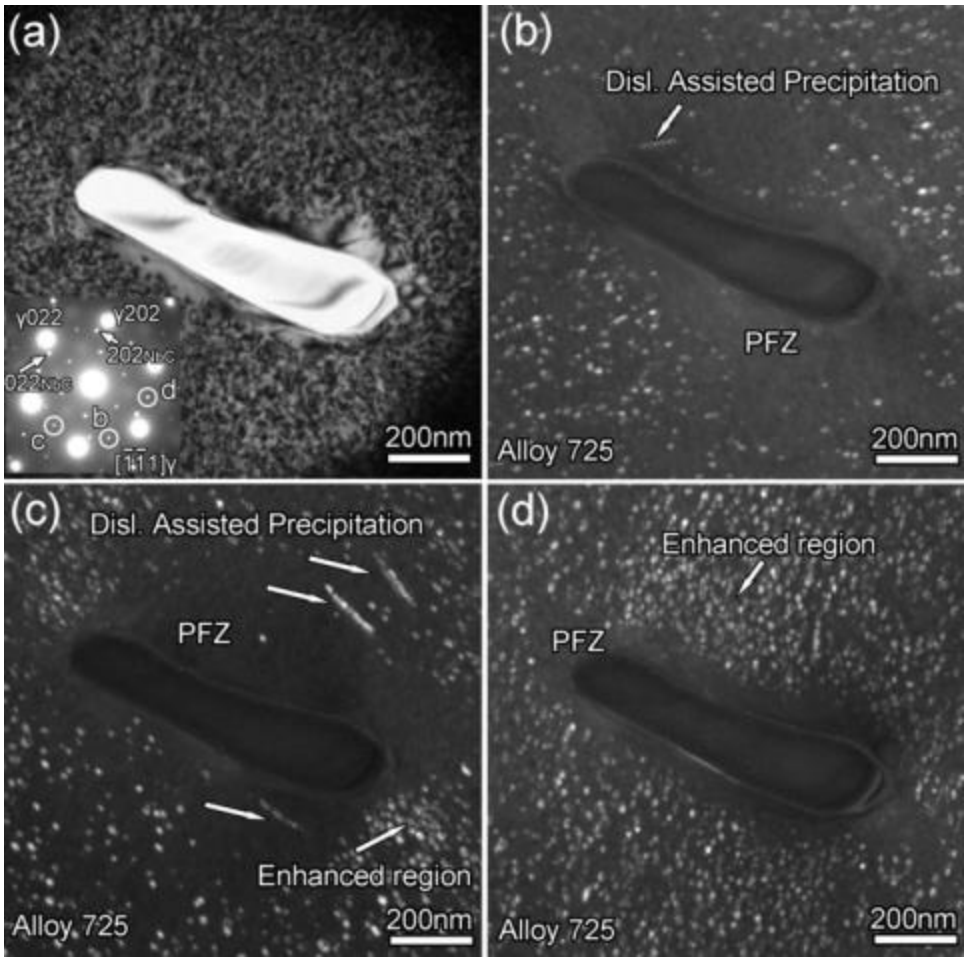

Figure 24. Variant dependent PFZ around a primary particle with zone axis [111]γ in alloy 725. (a) BF image of a primary particle with clearly PFZ around it. (c-d)Variant dependent PFZ was observed in [-1-11]γ zone axis. The morpholgy of three variants of γ'' phase should be similar in this direction with a 60 degree rotation. However, a much more complicated PFZ shape was observed due to the presence of primary particle. Dislocation assisted precipitation was noted.

3.3.1 Dislocation loops

Faulted, Frank loops are frequently observed in the irradiated austenitic steels [23, 24] and nickel-base alloys [25]. The habit plane is the {111} close packed plane. These loops are easily observed by the rel-rod method, which takes advantage of the diffraction pattern of stacking faults and creates a streaked line between the major diffraction spots. According to the crystallography of the FCC structure, only one quarter of the total loops is imaged, so the loop density was calculated by multiplying by a factor of 4.

Figure 25 shows a typical rel-rod image of dislocation loops in alloy 725, which is typical for all the alloys investigated. All the loops are inclined in the same direction as all of them share the same habit plane. The size distributions of loops for different alloys are shown in Figure 26.

The smallest loops were observed in alloy 625DA. The loops with the largest average size were observed in alloy 690. The size of the loops is determined by the stacking fault energy. Lower stacking fault energy encourages the formation of larger loops due to the larger separation distance between the

partial dislocations. The loop density is on the order of $10^{22}/cm^3$. Alloy 625 and alloy 625Plus have a similar density of dislocation loops, and both are greater than that of alloy 725.

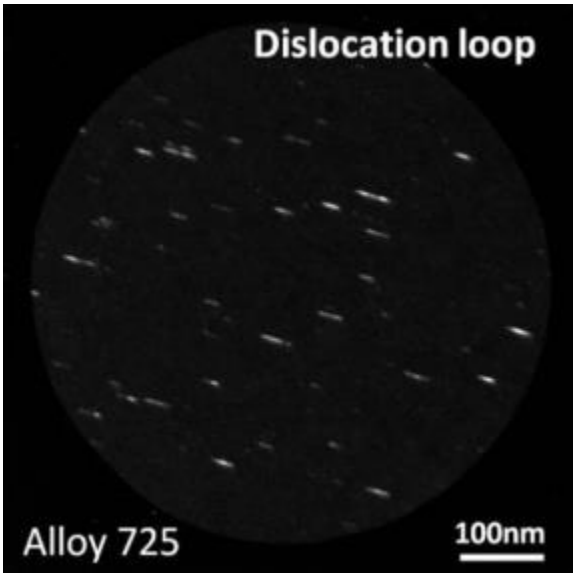

Figure 25 Faulted loops in alloy 725. These loops are observed through the rel-rod method. The alloys are irradiated at 360°C to around 5 dpa by protons.

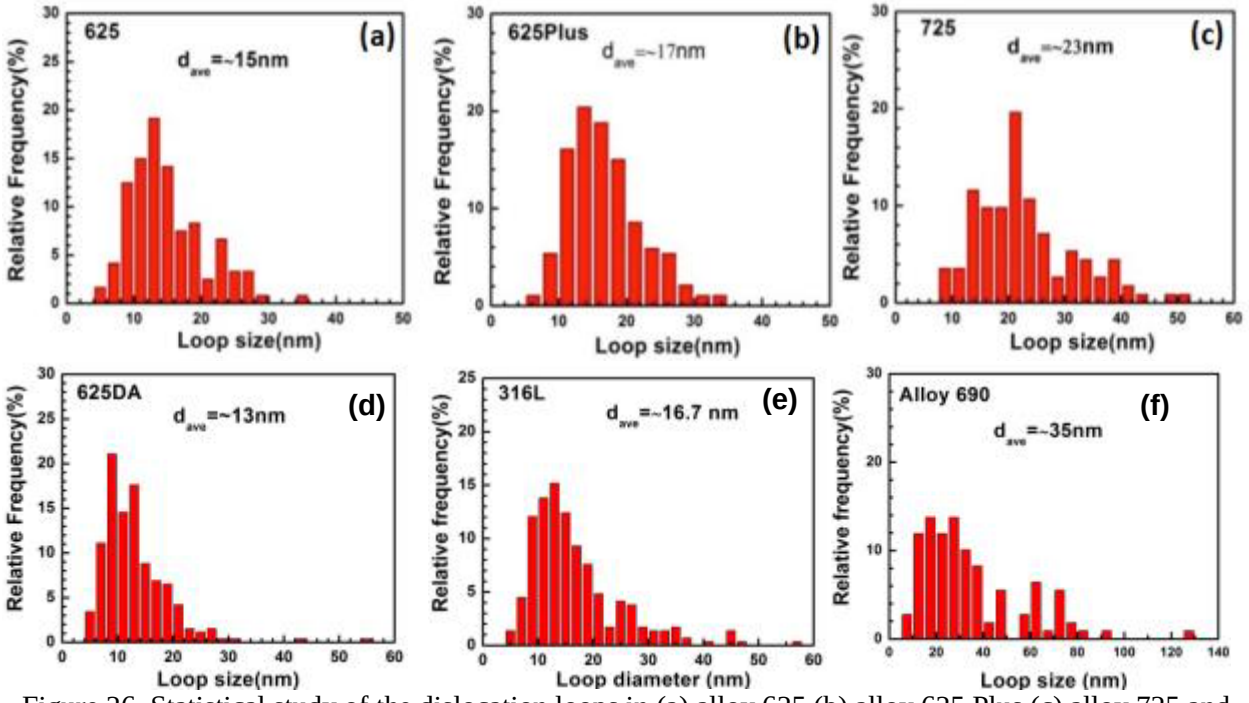

Figure 26. Statistical study of the dislocation loops in (a) alloy 625 (b) alloy 625 Plus (c) alloy 725 and (d) 625DA (e) 316L and (f) alloy 690. The largest loop size occurs in alloy 690. These alloys are irradiated at 360°C to about 5 dpa by protons.

3.3.2 Pre-existing precipitates

Irradiation can change the pre-existing precipitates by dissolution or disordering. It can also transform the pre-existing precipitates into precipitates of a different structure. However, no significant size and density change of γ'' phase was observed in the alloys studied. Part of the precipitates was not observed in the dark field, which were spots that deviated from the standard diffraction condition as shown in Figure 27. This could be due to partial re-solution of the phase that breaks the ordered structure. The average size was similar to those of the as-received materials for both alloy 625Plus and alloy 725 as shown in Figure 28. It was also noted that no precipitation of γ'' phase was observed in alloy 625, which did not have these precipitates previously.

3.3.3 Irradiation-induced or -enhanced precipitates

Long range ordering has been observed in various binary and ternary nickel-base alloy systems under thermal exposure [26-31]. In the alloy 625 family, the ordered phase is typically of a Pt_2Mo type structure with a body-centered orthorhombic structure. Some results show that this phase can also form after irradiation [32].

However, this phase was characterized for all nickel base alloy after irradiation. Taking alloy 725 as an example, a typical [001] zone axis is shown in the upper right corner of Figure 27a. The superlattice reflection at {100}, {110}, {1 ½ 0} are from the three variants of γ'' phase. Corresponding dark field images show the three variant of γ'' phase as previously observed in Figure 27b-d. In addition to this superlattice, another group of spots at 1/3{220} position were also observed in Figure 27a. These diffraction spots are associated with variants 1 and 2 of the Ni_2Cr phase, which is a long range ordered (LRO) phase. This phase has a total of six variants according to the symmetry of the crystallography. The six variants have an orientation relationship with the matrix as follows: variant 1 $(001)[110]_M//(001)[100]_{Ni2Cr}$ and variant 2 $(001)[1\text{-}10]_M//(001)[100]_{Ni2Cr}$, variant3 $(001)[011]_M//(001)[100]_{Ni2Cr}$ and variant 4 $(001)[0\text{-}11]_M//(001)[100]_{Ni2Cr}$, variant5 $(001)[101]_M//(001)[100]_{Ni2Cr}$, and variant 6 $(001)[10\ 1]_M$ // $(001)\ [100]_{Ni2Cr}$. Dark field images show the morphology of LRO phase in Figure 27e-f. These precipitates were randomly distributed within the matrix. There was no clear evidence that the formation of this LRO phase was associated with the pre-existing γ'' phase. No particular shape was observed for the LRO phase, so it was irregular shape.

The LRO phase was checked for almost all the alloys after irradiation as shown in Figure 29. As the Fe content increase, the diffraction spots of the LRO phase become weaker and weaker. In alloy 718, there is no diffraction spot can be identified related to the LRO phase. As the alloy come to the Fe rich part, the γ' phase becomes popular shown in Alloy 800 Figure 29g. The key of the diffraction pattern was given in Figure 29h. Three variants of LRO phase were observed in this direction and only a single variant of γ'' phase can be observed. Among different alloys, a bias of these LRO phases was observed in the selected area diffraction pattern (SADP) as shown in Figure 29. According to diffraction theory, the intensity of the diffraction spots relative to transmission spots can be an indicator of the relative amount of each phase. It was apparent that the diffraction spots of three variant were not of the same intensity in Figure 29a b and c. In Figure 29d, the diffraction spots representing three variants showed a similar intensity in alloy 725. In alloy 625Plus, diffraction spots for variant 4 and variant 6 showed a similar intensity while that for variant one showed weaker intensity. In alloy 625, the bias becomes even more significant. No diffraction spots of variant 1 were observed. Variant 6 became the dominant variant in the precipitation process. The precipitation of LRO phase showed equality among variants in alloy 725 and bias precipitation among variants in alloy 625Plus, 625DA and alloy 625. This effect is still not well understood and further effort is needed to unfold the underlying mechanism.

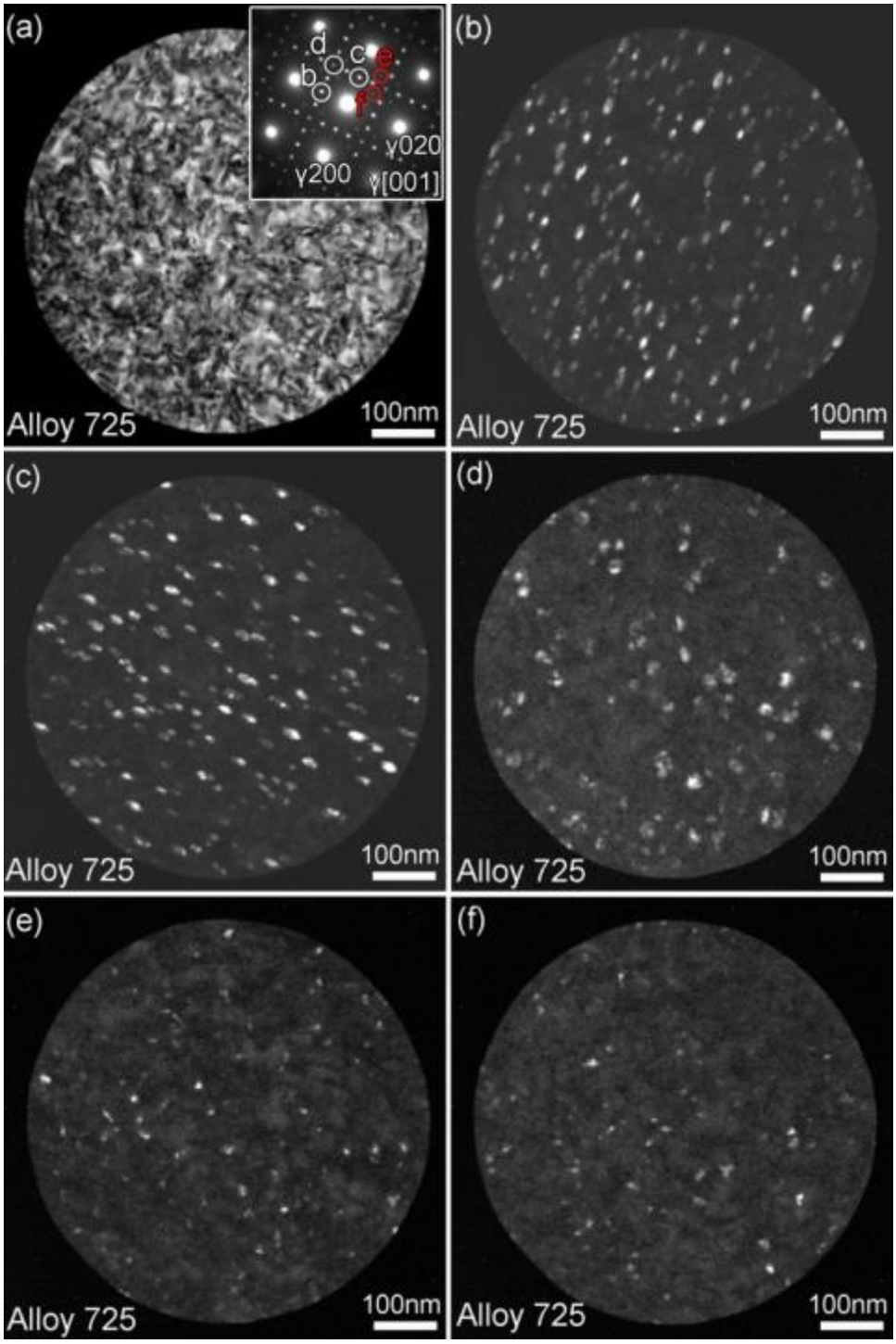

Figure 27. (a) Bright field (BF) and (b-d) dark field (DF) TEM images of γ'' precipitates after irradiation and irradiation induced long range order phase (e-f) in alloy 725. This alloy is irradiated at 360°C to about 5 dpa by protons.

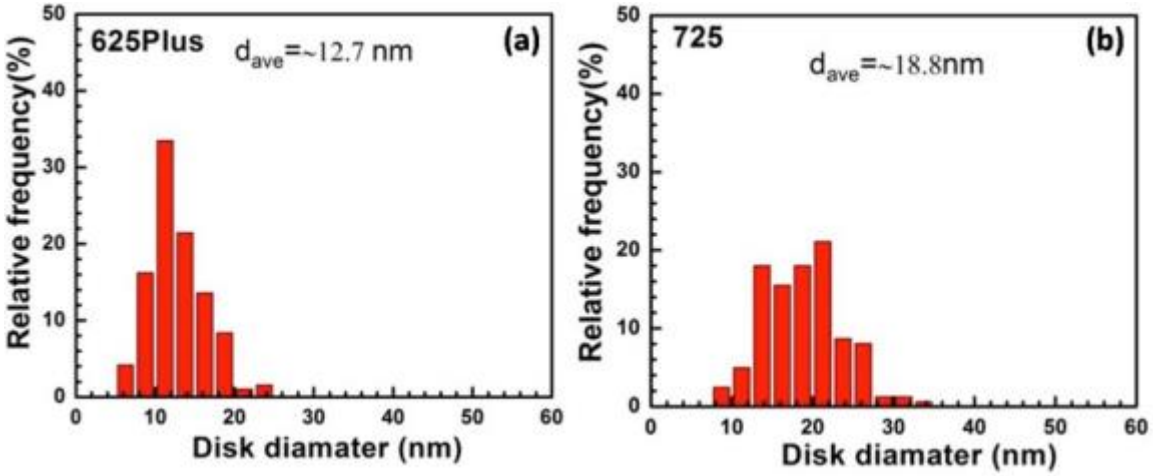

Figure 28. Statistical results of γ'' phase size distribution in (a) 625Plus and (b) alloy 725 after ~5dpa irradiation at 360°C by protons. No significant size change was noticed.

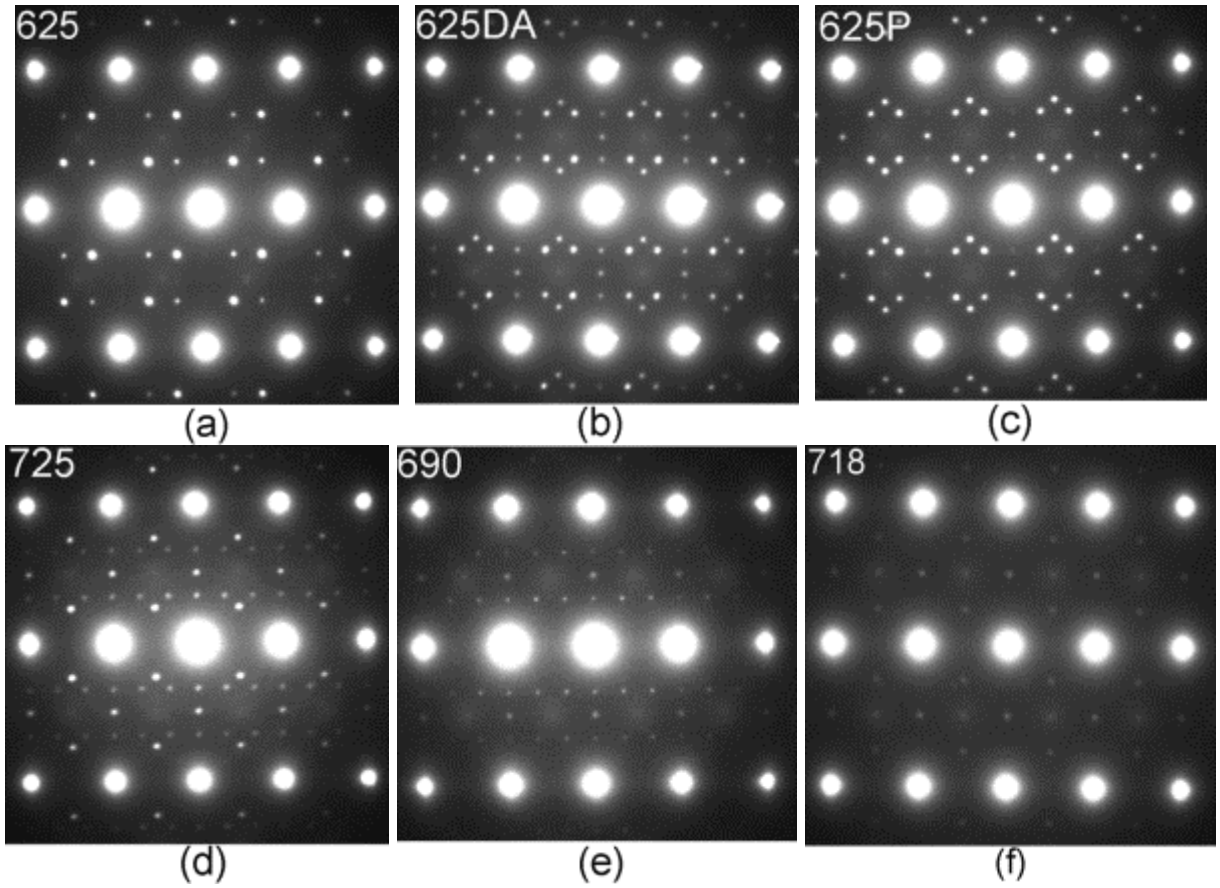

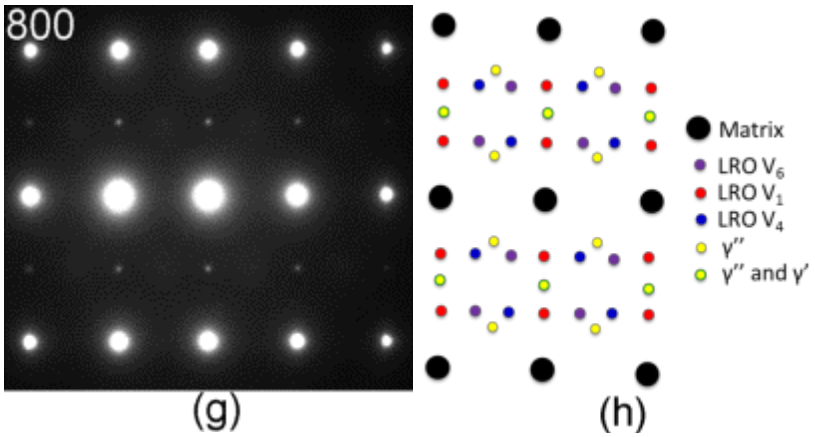

Figure 29. Diffraction patterns of the long range order phase (a)Alloy 625 after 5dpa (b) Direct Aged 625 after 5dpa (c) 625Plus after 5dpa (d) Alloy 725 after 5dpa (e) Alloy 690 after 5dpa (f) Alloy 718 after 4dpa (g) Alloy 800 after 5dpa (h) Key of the diffraciton pattern.

Statistical results of the size distribution for the LRO phase are listed in Figure 30. Larger size precipitates were observed in alloy 725, alloy 625DA and alloy 690. Smaller sizes of LRO phase were observed in alloys 625 and 625Plus. The difference in size of precipitates for alloy 625 and 625Plus was insignificant. It should be noted that the final size of these irradiation-induced precipitates was determined by the dynamic balance of irradiation-induced displacement and irradiation enhanced diffusion processes. It shows that the size varied with chemical composition of alloys while the influence of other intrinsic properties of the alloy is an open question.

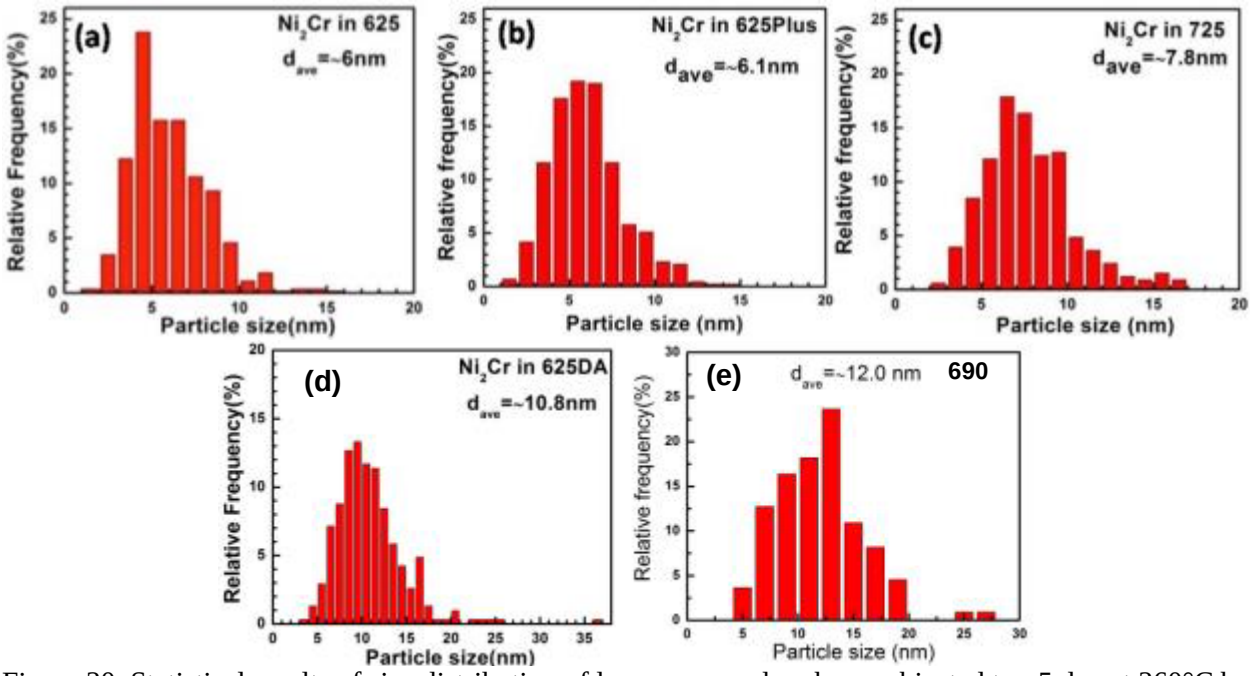

Figure 30. Statistical results of size distribution of long range-order phase subjected to ~5 dpa at 360°C by proton in (a) alloy 625 (b) alloy 625Plus (c) alloy 725(d)625DA and (e) alloy 690. These long range-order phases are Pt_2Mo type structure with major chemical composition of Ni_2Cr. The detailed chemical composition have yet to be determined.

3.3.4 Voids

Void swelling is a common phenomenon in irradiated materials [33]. It can change the dimension of the structure materials and significant residue stress may build up. Poor resistance to void swelling is a commonly issue for austenitic stainless steel at high dpa. Some of the austenitic stainless steel or model alloy can form voids even at low dpa levels [24]. Voids were identified in both 316L and 310 as shown in Figure 31. The voids in alloy 316L is in a round shape while the voids in alloy 310 are faceted. The statistical results of voids size distributions are shown in Figure 32. The average size of voids in alloy 310 is almost twice that in alloy 316L. No voids were observed for all the other alloys irradiated at the same condition.

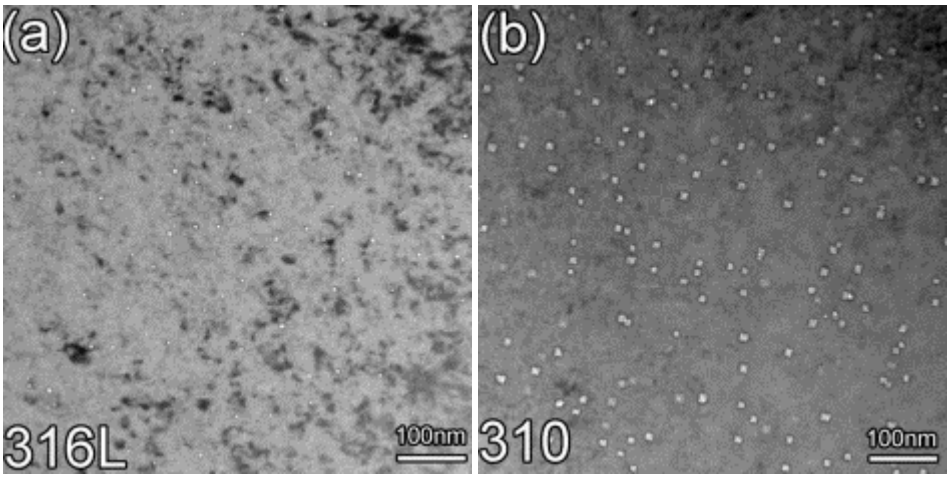

Figure 31.Voids in (a) alloy 316L and (b) alloy 310

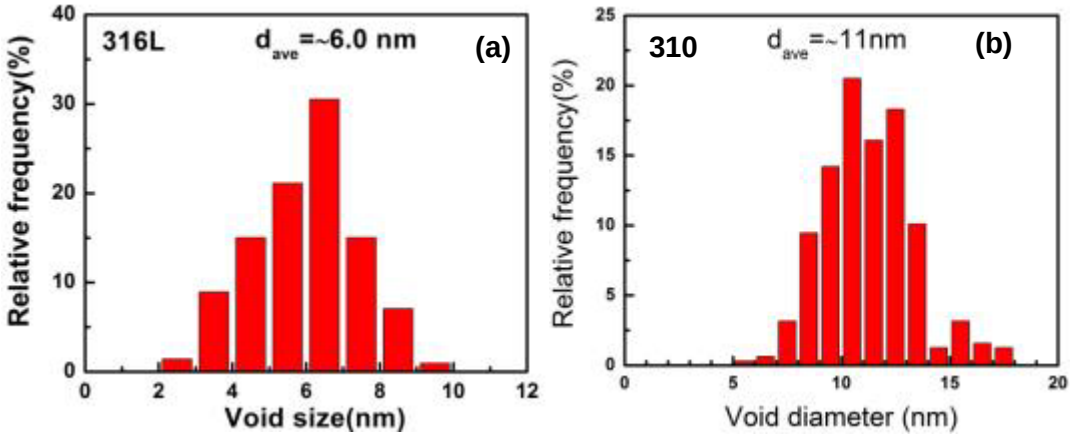

Figure 32. Voids distribution in (a) 316L and (b) 310 after 5dpa proton irradiation at 360°C

3.3.5 Irradiation induced segregation

Irradiation can significant increase the population of point defects far from equilibrium level. These point defects can migrate to the defect sinks such as free surface and grain boundary. This flux of point defects will change the elements around sinks which causes radiation induced segregation (RIS). The RIS process around GB is widely investigated around various alloy systems. RIS is one of the primary concerns for causing irradiation assisted stress corrosion cracking.

As shown in Figure 33, Significant Ni enhancement was observed in the nickel base alloy while Cr and Fe were always depleted. Mo was a slow diffuser which is enriched in the as received materials and diffuses away from GB. A comparison of RIS in nickel base alloy was summarized in Figure 34. 625DA shows the lowest GB Cr level around 8%. The nickel goes up to 70% which is around 10% above the bulk composition.

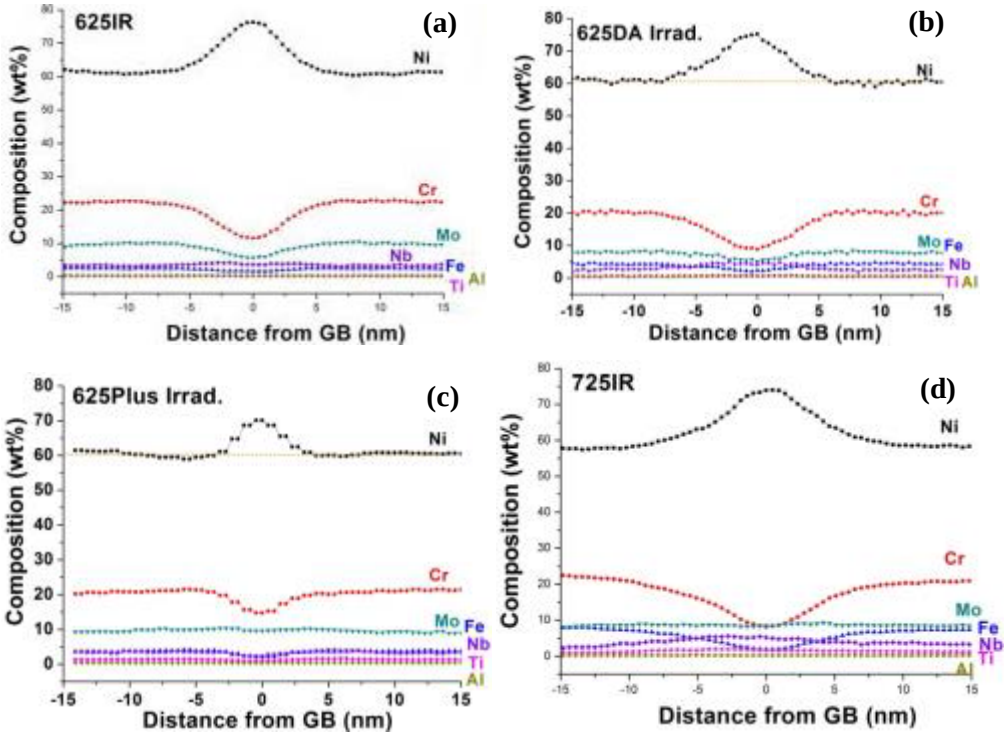

Figure 33. RIS in nickel base alloys (a) alloy 625 (b) alloy 625Plus (c) alloy 625DA and (d) alloy 725 after around 5 dpa proton irradaition at 360°C.

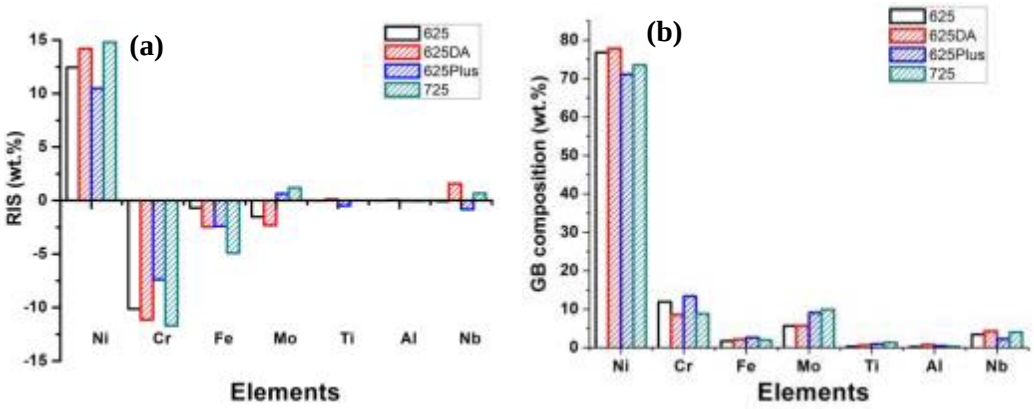

Figure 34. Comparision of (a) RIS and (b) GB chemical composition in nickel base alloys.

3.3.6 Summary of irradiated microstructure

Table 8 summarizes all the microstructure features of the alloys after proton irradiation to 5 dpa at 360°C. It was noted that the density of LRO phase in alloy 625 and alloy 625DA was an order of magnitude higher than that in alloy 725. The dislocation density of all the nickel base alloys was within an order of magnitude. Table 9 summarizes the RIS for all the alloys measured. All the major elements were listed.

Table 8. Effect of 2 MeV proton irradiation to 5 dpa at 360°C on the microstructure

	Pre-existing Precipitates						New formed precipitates			Dislocaation loops			Voids		
	before irradiation			after irradiation			d	ρ	fv	d	ρ	L	d	ρ	S %
	d	ρ	fv	d	ρ	fv									
	γ'' phase						Ni_2Cr type								
625	N/A	N/A	N/A	N/A	N/A	N/A	6.0±2.2	43±19	4.9	14.9±5.6	4.7±2.0	2.19	N/A		
625P	13±3.3	4.5±3.5	2.51	12.7±3.4	6.3±1.6	3.3	6.1±2.1	10.5±2.6	1.2	16.7±5.4	3.1±0.8	1.62	N/A		
725	18±6.0	2.9±1.2	3.69	18.9±4.7	2.3±0.9	3.2	7.8±2.6	2.0±0.9	0.5	23±8.7	1.4±0.6	1.01	N/A		
625DA	12±3.1	2.1±0.2	0.78	11.5±3.3	6.6±4.0	2.7	10.8±3.8	9.6±3.9	6.3	13±5.8	10.2±1.1	4.16	N/A		
690	N/A						12.0±4 γ' phase 5.6±2.0 γ' phase			34.6±21.7			N/A		
316	N/A						N/A			16.7±8.2			6.0±1.4		
310	N/A												11.2±2.1		
800	N/A														

Table 9. RIS for all the alloys examined (wt.%)

Alloy	Position	Ni	Cr	Fe	Mo	Ti	Al	Nb
625Plus	Matrix (wt. %)	60.65±0.77	20.79±0.50	5.00±0.76	8.50±0.49	1.43±0.12	0.52±0.12	3.11±0.32
	Avg.GB comp.(wt. %)	71.15±2.03	13.40±1.72	2.60±0.56	9.13±0.96	0.95±0.14	0.49±0.13	2.29±0.30
	RIS	10.49	-7.38	-2.40	0.64	-0.48	-0.03	-0.83
625DA	Matrix (wt. %)	63.67±0.045	19.70±0.70	4.62±0.30	8.02±0.04	0.56±0.04	0.70±0.13	2.74±0.24
	Avg.GB comp.(wt. %)	77.86±0.32	8.56±0.87	2.15±0.34	5.70±0.68	0.68±0.05	0.75±0.07	4.30±0.10
	RIS	14.19	-11.14	-2.47	-2.32	0.12	0.048	1.56
625	Matrix (wt. %)	64.38±1.70	22.05±0.97	2.39±0.12	7.20±2.72	0.28±0.03	0.22±0.07	3.48±0.03
	Avg.GB comp.(wt. %)	76.82±0.09	11.92±0.43	1.70±0.05	5.68±0.04	0.27±0.03	0.20±0.12	3.41±0.38
	RIS	12.45	-10.13	-0.69	-1.52	-0.02	-0.02	-0.06
725	Matrix (wt. %)	58.79±0.76	20.52±0.45	6.92±0.66	8.72±0.35	1.35±0.07	0.32±0.11	3.39±0.17
	Avg.GB comp.(wt. %)	73.58±1.73	8.83±1.02	1.99±0.25	9.91±2.73	1.35±0.31	0.26±0.07	4.07±1.24
	RIS	14.80	-11.69	-4.92	1.19	0.003	-0.058	0.68

3.4 Mechanical Properties

3.4.1 Irradiation hardening

Hardness measurements of each alloy before and after irradiation are listed in Table 9 and plotted in Figure 35. Alloys 625Plus, 625DA and 725 are precipitate-strengthened nickel-base alloys and had a similar Vickers microhardness of around 425 Hv before irradiation. Alloy 625 is a solid solution alloy and thus it had the relative low Vickers microhardness, about 346 Hv before irradiation. Alloy 316L and alloy 690 have even lower hardness. Alloy 800 was the softness materials with the Vickers hardness around 154. Significant hardening up to 90% was observed in alloys 316L, 800, and 690. The alloys from 625 families show moderate irradiation hardening. The F/M steel T92 shows very small amount of hardening.

Table 9. Microhardness Measurement before and after irradiation.

Alloy	Pre-irradiation (Hv)	Post-irradiation (Hv)
625	346 ± 24.5	447 ± 20.4
625Plus	424 ± 22.5	482 ± 24.4
725	428 ± 17.8	526 ± 18.8
625DA	420 ± 16.0	577± 28.0
316L	201± 18	386±22.4
800	154±12.2	292±25
690	198±12	345±27
T92	254±12.1	281±18

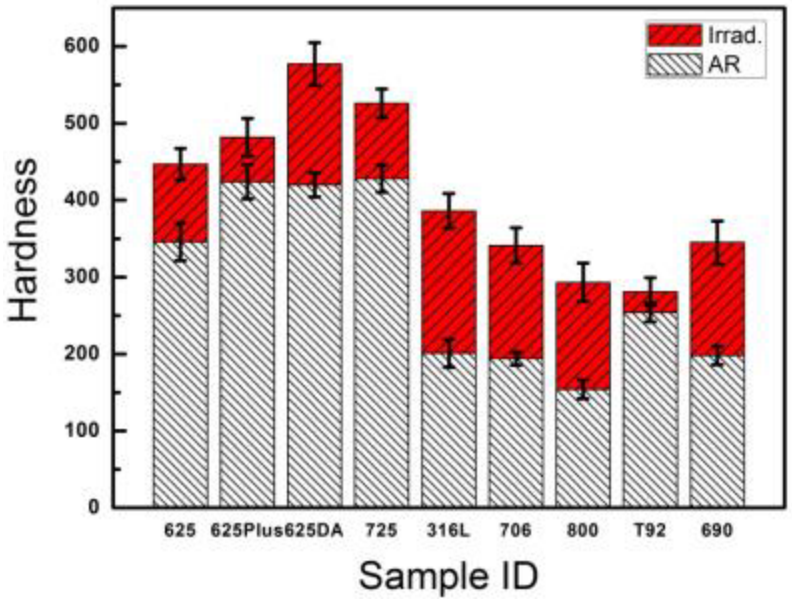

Figure 35. Irradiation induced hardening in various materials upto 5dpa at 360°C

3.4.2 Room temperature tensile behavior

Tensile test results of alloy 625 family were plotted in Figure 36a. The alloy 725 shows the highest yield stress and ultimate tensile stress. Alloy 625 without any precipitate hardening shows the lowest yield strength but high ductility. The working hardening rate was evaluated in Figure 36b. The highest work hardening rate was observed in alloy 725. Alloy 625DA and alloy 625 show similar stress-strain curves and similar work hardening behavior. Alloy 625 shows the lowest work hardening rate at a given stress. Alloys 625 and 718 have similar working hardening stages. The work hardening stage two is very short for alloy 625Plus, 625DA and alloy 725. All the mechanical properties were tabulated in Table 10.

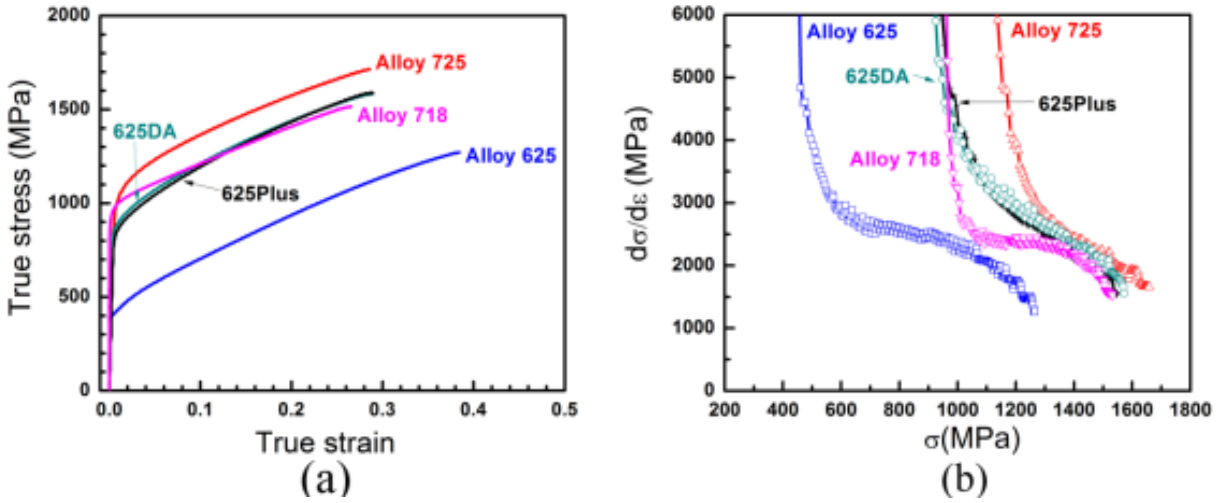

Figure 36. Comparison of stress-strain curves of different precipitates-hardened nickel base alloys. (a) True stress vs. true strain. (b) Hardening rate dσ/dε vs true stress.

Table 10. Mechcanical properties of nickel base alloys

Alloy	Elastic Modulus (GPa)	Yield Strength (MPa)	Ultimate Tensile Strength (MPa)	Plastic Strain at UTS (mm/mm)
625	227	400	868	0.454
625DA	213	867	1194	0.310
625Plus	198	825	1199	0.310
725	206	986	1296	0.289

3.5 CERT Test Results

The CERT tests for nickel-base alloys 625 (5 dpa), alloy 625DA, alloy 625Plus (4.15 dpa), and alloy 725 (5 dpa) in both BWR NWC and PWR primary water environments were completed. Table 11 summarizes the results of the CERT tests. The stress-strain curve of alloy 725 as an example is shown in Figure 37.

All alloys were strained to a plastic strain close to 4%. Alloy 725 had the highest yield strength among all the high strength alloys at high temperature, 625Plus and 625DA were at the same stress levels which was in agreement with the tensile test at room temperature. Because less than 1% of the thickness of the alloy was actually irradiated by the proton beam (20 μm irradiation depth over 2 mm bar thickness), the yield strengths obtained were not expected to show any effect of irradiation. The serrations in the plastic deformation region were due to the dynamic strain aging of the alloys.

Table 11. CERT resutls summary of nickel base alloys in both BWR NWC and PWR primary water environments, NM: not measured.

Alloy (Dose)		Env.	Yield Strength (MPa)	Plastic strain by LVDT (%)	Plastic Strain (%) from fiducial marks
High Strength	**725 (5dpa)**	PW-1	923 ± 10	4.1 ± 0.1	3.8
		PW-2	911 ± 19	4.25 ± 0.2	4.1
		NWC-1	890 ± 17	3.7 ± 0.1	NM
		NWC-2	874 ± 13	3.9 ± 0.1	3.8
	625Plus (4.15dpa)	PW-1	740 ± 7	4.25 ± 0.1	4.0
		PW-2	732 ± 9	4.15 ± 0.2	3.9
		NWC-1	730 ± 17	3.6 ± 0.1	NM
		NWC-2	713 ± 9	4.0 ± 0.1	3.9
	625DA (5dpa)	PW-1	732 ± 11	3.9 ± 0.2	3.8
		PW-2	767 ± 13	4.2 ± 0.1	4.0
		NWC-1	760 ± 11	4.0 ± 0.1	3.8
		NWC-2	830 ± 11	4.55 ± 0.1	4.4
Low Strength	**625 (5dpa)**	PW-1	365 ± 9	4.05 ± 0.1	NM
		PW-2	327 ± 8	4.2 ± 0.1	4.0
		NWC-1	326 ± 8	3.45 ± 0.1	NM

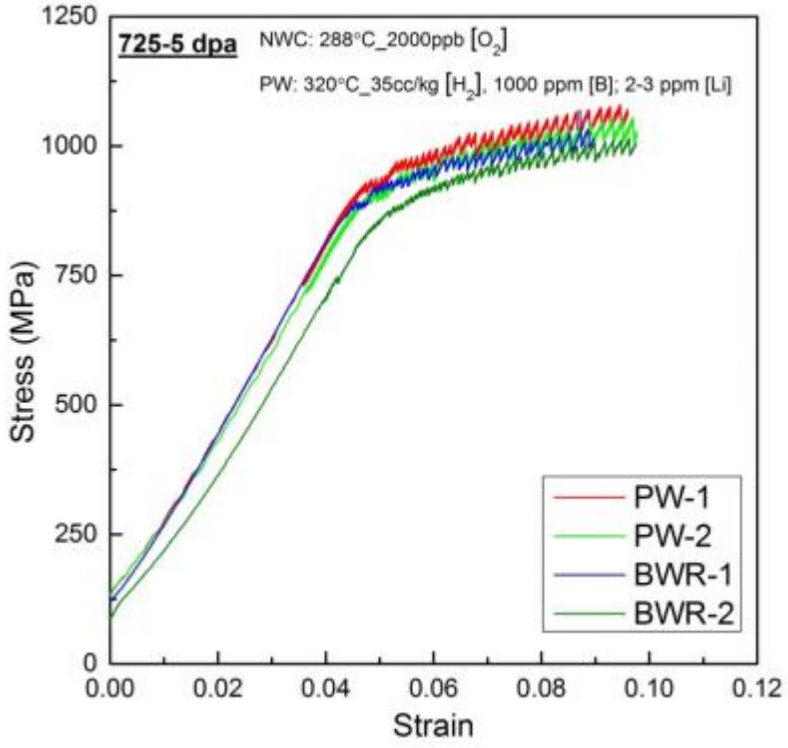

Figure 37. Stress-strain curve of alloy 725 (5dpa) in both BWR NWC and PWR primary water environments.

3.6 Cracking Behavior

3.6.1 General observation

3.6.1.1 Cracking on the irradiated surface

Small heterogeneous oxide crystallites were formed over the entire sample surface. In general, the oxide formed on nickel-base alloys should consist of a duplex oxide: an inner layer of continuous Cr-rich oxide with a discontinuous external layer with composition, morphology and microstructure depending on the environment and exposure duration [34, 35]. However, most of the external oxide should be an iron-rich spinel oxide, typically of the form of $Ni_{1-x}Fe_{2+x}O_4$, which may be the small crystallites observed on the surface [36-38].

Intergranular cracks were found on all the nickel base alloys in both BWR NWC and PWR primary water environments. Depending on the alloy and environment, cracking behavior varies accordingly. One SEM micrograph of alloy 625Plus (4.15dpa) strained to ~4% in BWR NWC is shown in Figure 38 as an example. Long cracks were clear and visible at this low magnification. Figure 39 and Figure 40 show the cracks found in the irradiated area of alloy 625Plus, alloy 725, alloy 625DA, and alloy 625 in BWR NWC and PWR primary water, respectively.

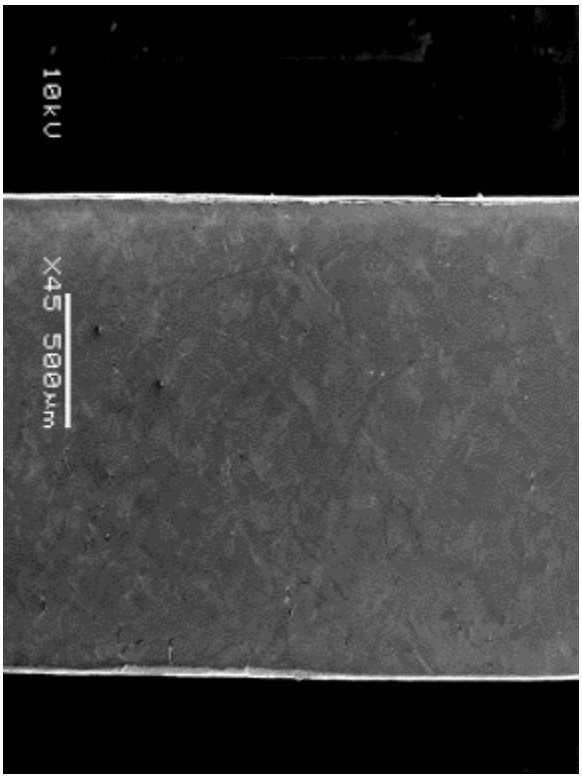

Figure 38. Low magnification SEM micrograph in the irradiated area (IA) of the tensile sample of alloy 625Plus irradiated to a dose of 4.15 dpa and strained to ~ 4% in BWR NWC environment.

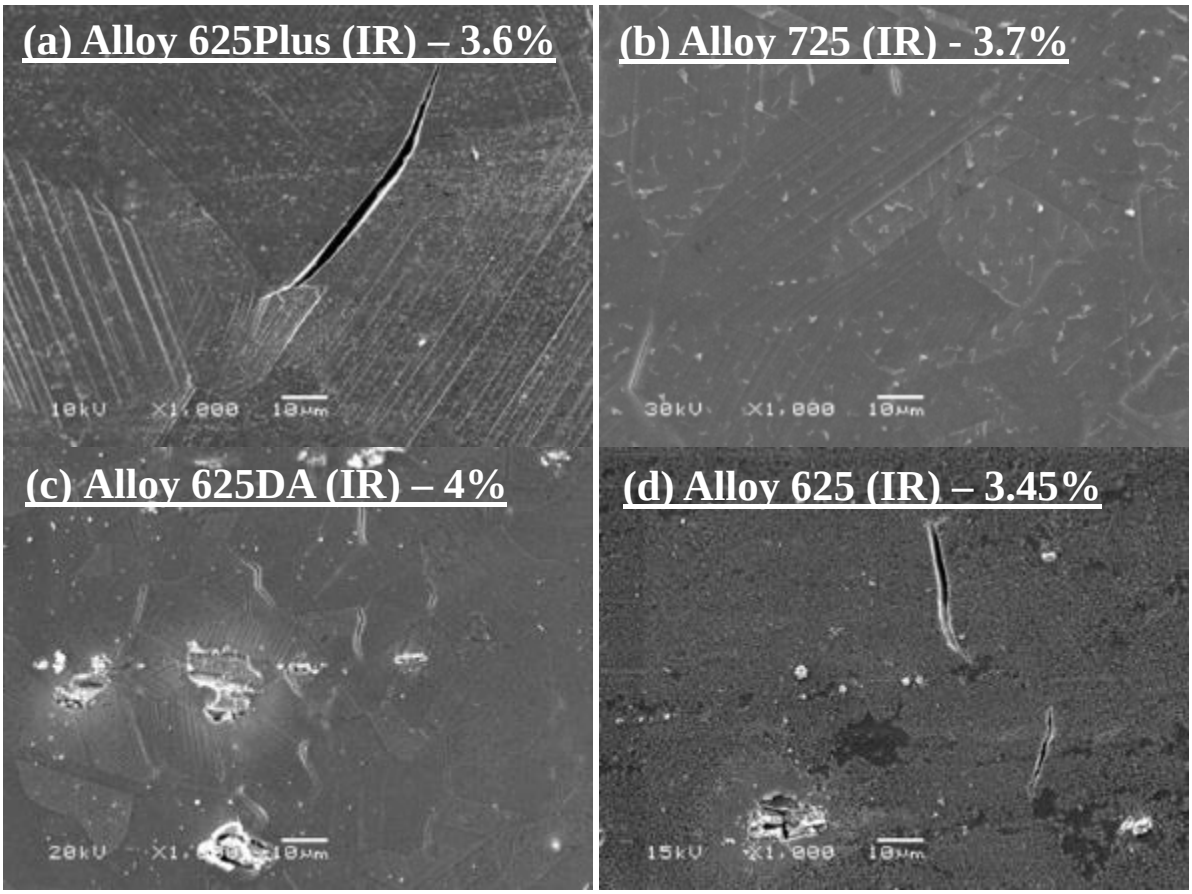

Figure 39. SEM micrograph in the irradiated area (IA) of the tensile sample: (a) alloy 625Plus, (b) alloy 725, (c) alloy 625DA, and (d) alloy 625, irradiated to a dose of ~5 dpa and strained to ~ 4% in BWR NWC environment.

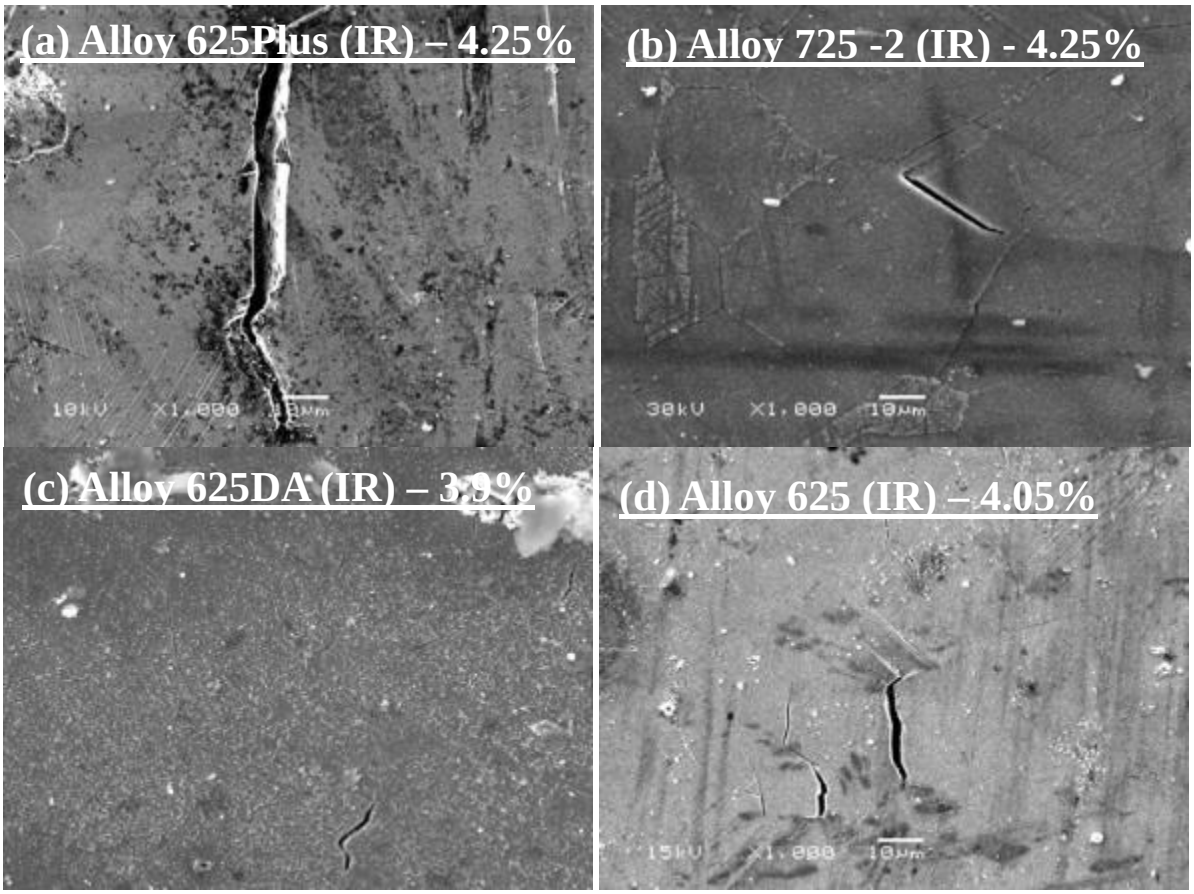

Figure 40. SEM micrograph in the irradiated area (IA) of the tensile sample: (a) alloy 625Plus, (b) alloy 725, (c) alloy 625DA, and (d) alloy 625, irradiated to a dose of ~5 dpa and strained to ~ 4% in PWR primary water environment.

3.6.1.2 Comparison between irradiated area (IA) and unirradiated area (UIA)

Irradiation had a significant effect on cracking behavior of the alloys. In short, it enhanced the cracking susceptibility in both BWR NWC and PWR primary water environments. However, cracks were still found on the unirradiated areas. The comparisons between the two regions, irradiated area (IA) and unirradiated area (UIA), of each alloy in BWR NWC environment are shown in Figure 41, Figure 42, Figure 43, and Figure 44. For different alloys, different magnifications were chosen to show the cracks more clearly. From the observation, it showed that cracks were observed in both IA and UIA for alloy 625Plus, alloy 725, alloy 625DA, and alloy 625:

- The number of cracks in the IA was greater than that in the UIA;
- Crack opening was greater in the irradiated area (several microns) compared to the unirradiated area (less than 1 micron).

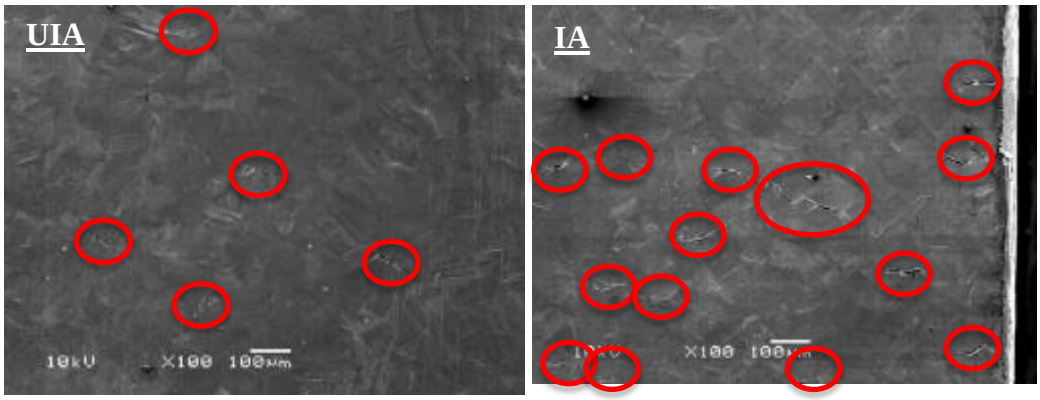

Figure 41. SEM micrographs of alloy 625Plus irradiated to a dose of 4.15 dpa and strained to ~ 4% in BWR NWC environment: unirradiated area (left) and irradiated area (right). Cracks were highlighted in red circles.

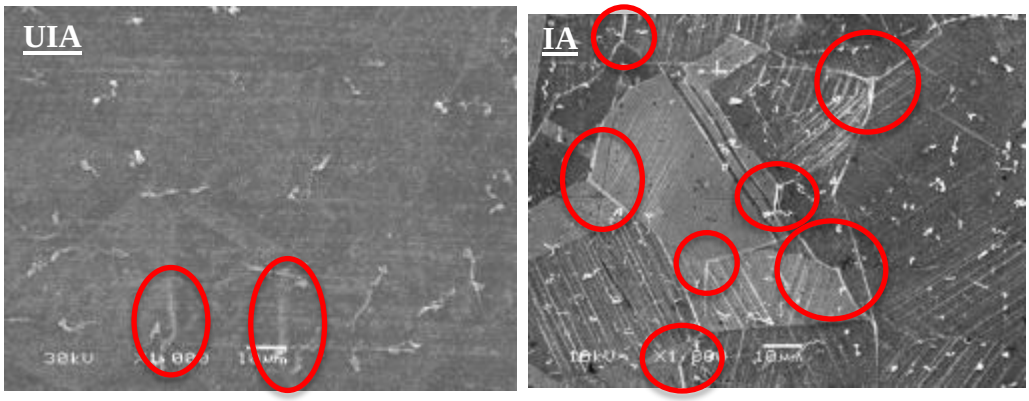

Figure 42. SEM micrographs of alloy 725 irradiated to a dose of 5 dpa and strained to ~ 4% in BWR NWC environment: unirradiated area (left) and irradiated area (right). Cracks were highlighted in red circles.

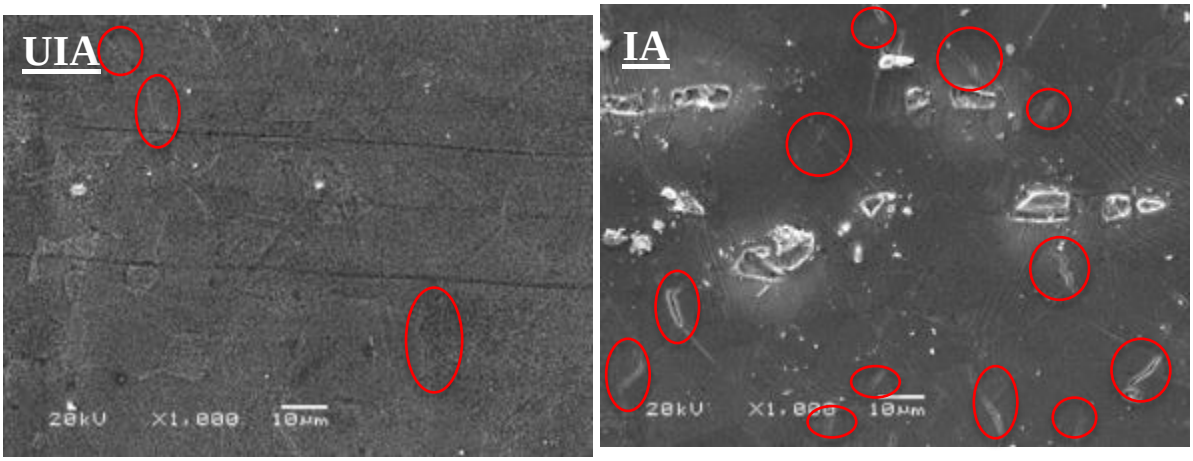

Figure 43. SEM micrographs of alloy 625DA irradiated to a dose of 5 dpa and strained to ~ 4% in BWR NWC environment: unirradiated area (left) and irradiated area (right). Cracks were highlighted in red circles.

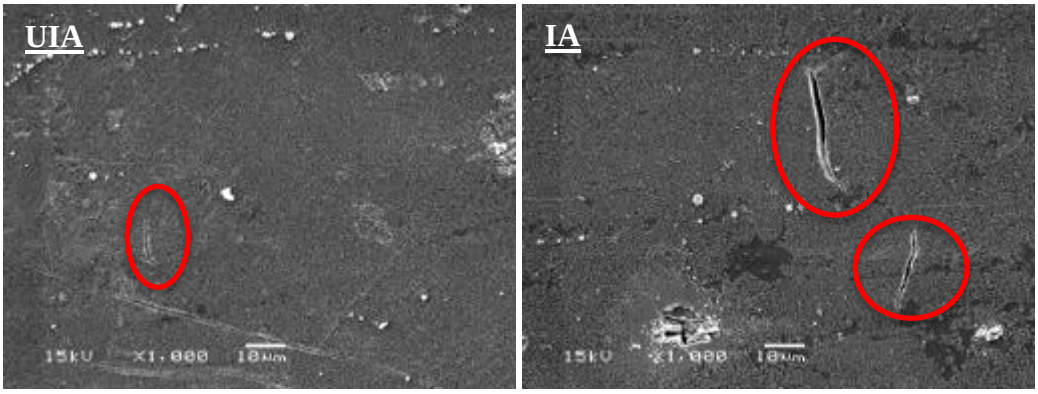

Figure 44. SEM micrographs of alloy 625 irradiated to a dose of 5 dpa and strained to ~ 4% in BWR NWC environment: unirradiated area (left) and irradiated area (right). Cracks were highlighted in red circles.

3.6.2 Crack characterization

SEM images were taken over similar size areas (approximately 1 mm^2) in both irradiated and unirradiated areas of the tensile sample. Only intergranular cracks were considered for the measurement.

Crack characterization for each condition including the following parameters:

- Average crack length;
- Crack density: the number of crack observed per unit area;
- Crack length per unit area: the total crack length divided by the analyzed area;

Table 12 shows the results of crack parameters for the nickel base alloys for both the unirradiated area (UIA) and the irradiated area (IA).

For average crack length:

- The average crack length in BWR NWC was usually larger than the one in PWR primary water for each alloy.
- The average crack length was more or less depended on the grain size of each alloy. The one had larger grain usually also had a longer average crack length. Among all the alloys, alloy 625Plus had the longest average crack length in both the irradiated and unirradiated areas.

For crack density:

- Alloy 625DA had the highest crack density in both irradiated and unirradiated areas among all the alloys;
- Alloy 725 had a very slight change in crack density between the unirradiated area and irradiated area while the 625DA had the greatest changes.

The most representative metric is crack length per unit area, which measures the extent of cracking by incorporating both the density and the length of cracks. For all the alloys, the crack length per unit area was much higher in the irradiated area than in the unirradiated area. Specifically, alloy 625DA, the most susceptible alloy to IASCC in both BWR NWC and PWR primary water environments. Alloy 725, on the other hand, had the lowest cracking susceptibility. Alloy 625Plus and low strength alloy 625 were also highly susceptible to IASCC.

To normalize the influence of grain size, the last parameter took into consideration was the crack length/unit area normalized to grain boundary length/unit area which was the fraction of grain boundary length that cracked. Under this standard, alloy 625Plus had the highest percentage of cracked grain

boundary among all while alloy 725 still had the lowest value in BWR NWC environment. Alloy 625DA, had the smallest grain size, thus had a lower crack percentage than alloy 625Plus in both environments and alloy 725 in PWR primary water environment. This parameter was helpful to describe the cracking behavior, however, the crack length/unit area was still the most important parameter to evaluate the IASCC susceptibility.

Table 12. Crack susceptibility of alloy 625Plus, alloy 725, alloy 625DA, and alloy 625 irradiated to a dose ~ 5 dpa and strained to ~ 4% in both BWR NWC and PWR primary water environments.

Alloy (Dose)		Env.	Area	Cracks counted	Average crack length (μm)	Crack density (#Cracks/mm^2)	Crack length/unit area (μm/mm^2)	Cracked length/ HAGB length (%)
High Strength	**625Plus (5dpa)**	PW-1	UIA	83	6 ± 1	89 ± 0.5	503 ± 47	3.33 ± 0.09
			IA	244	11 ± 1	263 ± 2	2895 ± 239	19.15 ± 0.08
		PW-2	UIA	94	11 ± 1	101 ± 1	1069 ± 131	7.07 ± 0.12
			IA	186	17 ± 1	200 ± 1	3465 ± 265	22.92 ± 0.08
		NWC-1	UIA	28	12 ± 2	30 ± 0.2	364 ± 160	2.41 ± 0.44
			IA	204	26 ± 2	171 ± 1	4502 ± 291	29.78 ± 0.07
		NWC-2	UIA	110	11 ± 1	118 ± 1	1295 ± 147	8.56 ± 0.11
			IA	210	15 ± 1	226 ± 1	3377 ± 280	22.33 ± 0.08
	725 (5dpa)	PW-1	UIA	111	5 ± 0.3	119 ± 1	609 ± 37	1.80 ± 0.06
			IA	118	6 ± 0.4	127 ± 1	711 ± 48	2.10 ± 0.07
		PW-2	UIA	78	8 ±1	106 ± 1	807 ± 90	2.38 ± 0.11
			IA	84	8 ±1	114 ± 1	968 ± 73	2.86 ± 0.08
		NWC-1	UIA	41	8 ±1	44 ± 0.3	365 ± 47	1.08 ± 0.13
			IA	191	9 ± 1	206 ± 1	1847 ± 129	5.45 ± 0.07
		NWC-2	UIA	60	14 ±1	131 ± 1	875 ± 89	2.58 ± 0.10
			IA	154	18 ± 1	166 ± 1	2967 ± 196	8.75 ± 0.07
	625DA (5dpa)	PW-1	UIA	66	6 ± 0.4	426 ± 3	2676 ± 177	0.96 ± 0.07
			IA	117	7 ± 0.4	756 ± 5	5620 ± 332	2.01 ± 0.06
		PW-2	UIA	182	7 ± 0.3	588 ± 4	4067 ± 148	1.46 ± 0.04
			IA	316	8 ± 0.4	1020 ± 6	8127 ± 421	2.91 ± 0.06
		NWC-1	UIA	97	10 ± 0.5	292 ± 2	2792 ± 150	1.00 ± 0.05
			IA	526	13 ± 0.4	1982 ± 11	25196 ± 862	9.02 ± 0.09
		NWC-2	UIA	166	8 ± 0.3	1072 ± 7	8785 ± 355	3.14 ± 0.03
			IA	481	9 ± 0.3	3107 ± 20	28632 ± 900	10.25 ± 0.03
Low Strength	**625 (5dpa)**	PW-1	UIA	19	5 ± 1	20 ± 0.1	103 ± 10	0.12 ± 0.10
			IA	403	9 ± 0.4	434 ± 3	3672 ± 171	4.28 ± 0.05

NWC-1	UIA	61	8 ± 1	66 ± 0.4	503 ± 41	0.57 ± 0.08
	IA	217	12 ± 1	234 ± 1	2728 ± 152	3.10 ± 0.06

The crack length per unit area of high strength nickel base alloys are plotted in Figure 45 and Figure 46 for BWR NWC and PWR primary water environments, respectively. The percentage of cracked length over grain boundary length are also plotted in Figure 47 and Figure 48 for BWR NWC and PWR primary water environments, respectively. It is clear that the cracking susceptibility of high strength nickel base alloys was much higher in BWR NWC than PWR primary water. It can be explained by the much oxidative environment created in BWR NWC environment causing the acceleration of cracking.

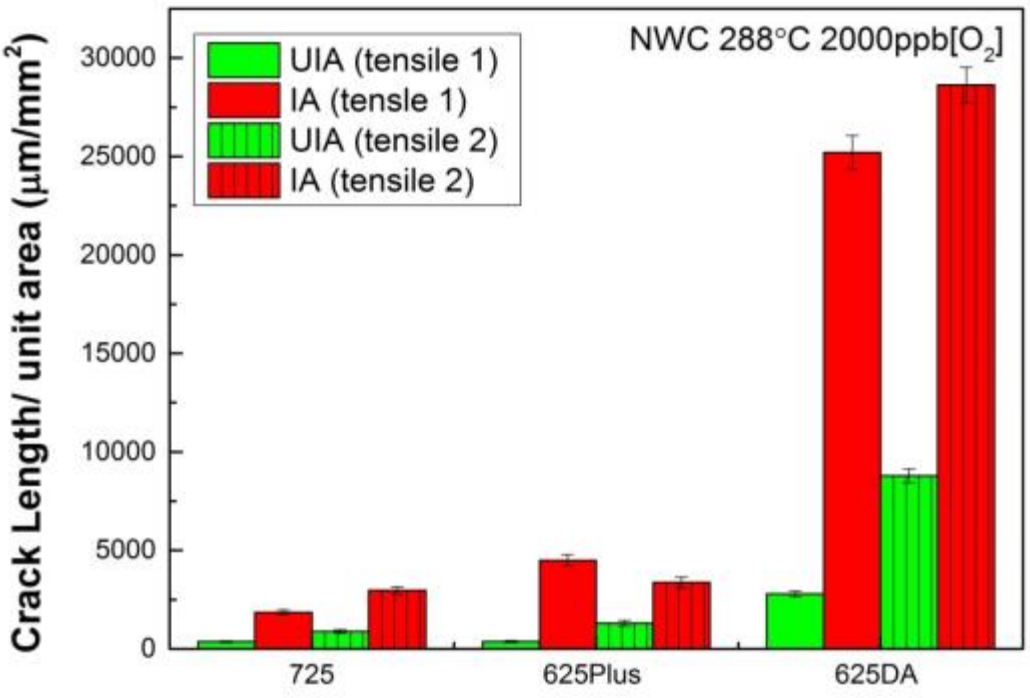

Figure 45. Cracking susceptibility of high strength nickel base alloys in BWR NWC environment.

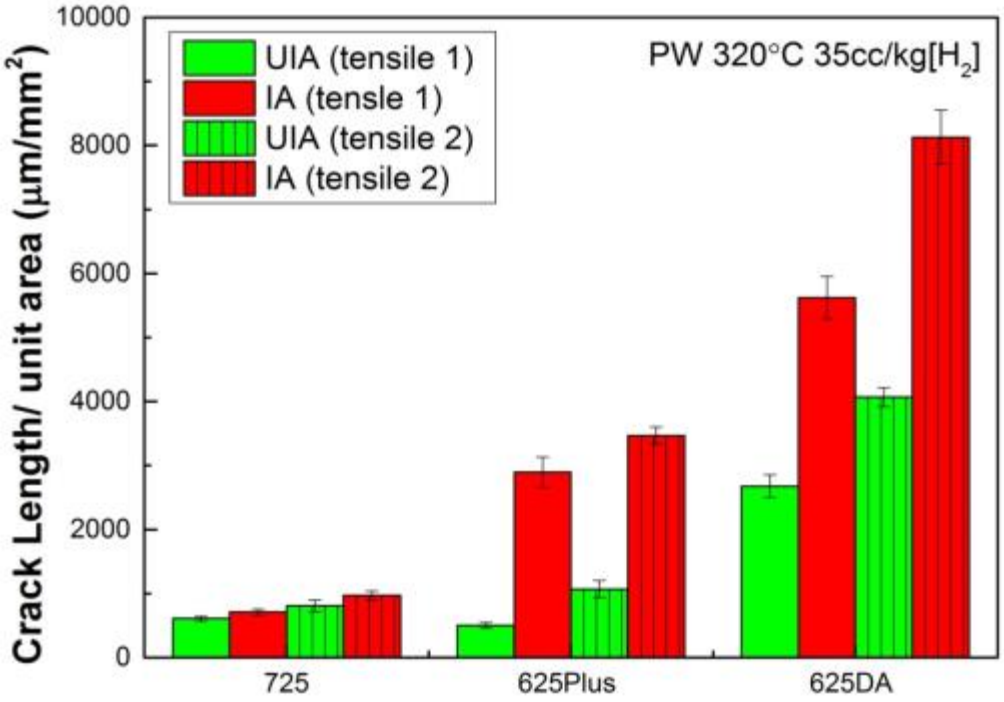

Figure 46. Cracking susceptibility of high strength nickel base alloys in PWR primary water environment.

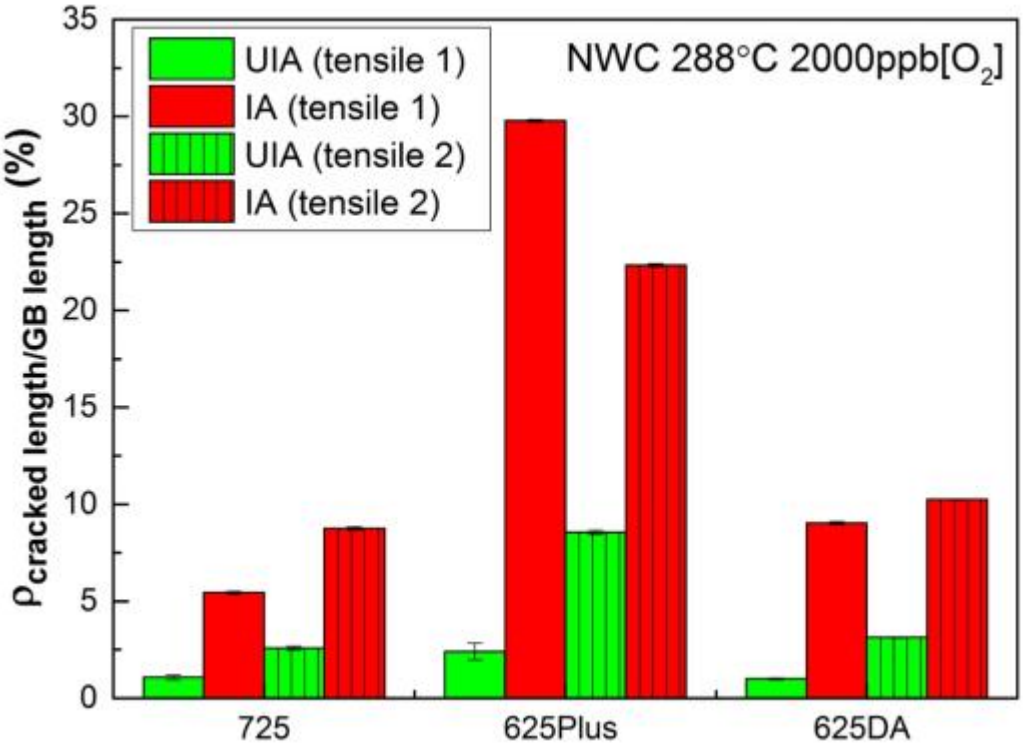

Figure 47. The ratio between cracked length and GB length of high strength nickel base alloys in BWR NWC environment.

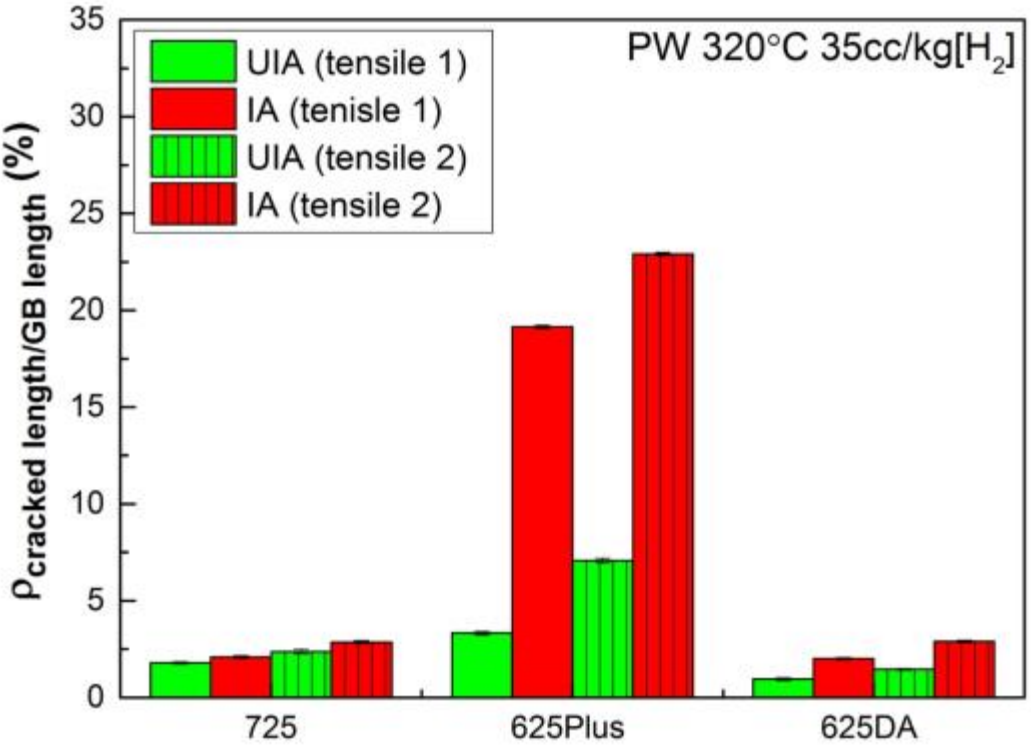

Figure 48. The ratio between cracked length and GB length of high strength nickel base alloys in PWR primary water environment.

To summarize, alloy 625DA was the most susceptible nickel base alloy to IASCC in LWR environment. Combining with the microstructure characterization after irradiation, 625DA was the alloy had the greatest irradiation induced microstructure changes. Figure 49 illustrates the ranking of IASCC behavior and microstructure changes after 5 dpa proton irradiation.

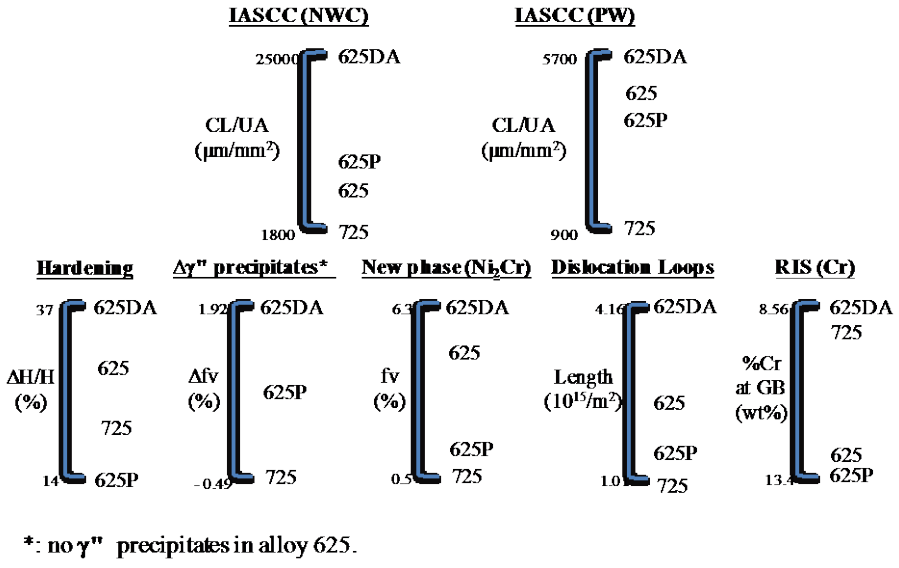

Figure 49. Ranking of IASCC behavior and microstructural changes after irradiation.

4. CONCLUSIONS

Over the period between September 2014 and September 2016, proton irradiations were conducted on commercial alloys including alloy 625, alloy 625Plus, alloy 625 Direct Aged (DA), alloy 725, Types 310, alloy 316, alloy 800 and alloy 690 and T92. The report will focus on the as received microstructure, irradiated microstructure, irradiation hardening, radiation induced segregation (RIS) and irradiation assisted stress corrosion cracking (IASCC) of these alloys. Pre-characterization of these materials was performed to identify the phase structure and evaluate the homogeneity of as-received materials. Post-irradiation analysis, irradiation hardening and CERT test were performed to evaluate the response of the alloys to proton irradiation and to evaluate their radiation resistance. Major findings are as follows:

- The chemical composition and heat treatment showed a significant impact on the microstructure of as-received materials. The as-received materials were generally homogenous in these alloys.
    - Stringers were observed in the extrusion direction in all alloys. The particles were identified to be (Nb,Ti) (C,N). The stringers in alloys 625DA and 625 were more pronounced than in alloy 625Plus and alloy 725. Between alloy 625 and alloy 625DA, alloy 625DA has the higher stringer content. The lower annealing temperature for alloy 625DA and 625 was likely a factor in the stringer content and distribution.
    - γ'' phase was observed in alloy 625Plus, 625DA and alloy 725. The γ'' precipitates were disk-shaped. The average diameter and thickness of precipitate in alloy 725 were larger than those of precipitates in alloy 625Plus and alloy 625DA. The high nickel content of alloy 625Plus and 625DA caused a lower stacking fault energy, which played a predominant role in the size of the precipitates. The lower Ti content in alloy 625DA resulted in a lower density of precipitates. The precipitation of γ'' was homogenous throughout the matrix except around primary NbC particles. The variant dependent precipitate free zones were first observed in these nickel-base alloys around primary particles. The interaction energy arising from thermal stress controlled the size of PFZs.
    - No intragrannular precipitates were identified in the as received 316L, 310, 800 and 690. However, GB carbides were frequently observed in these alloys.
- Alloy 725 and alloy 690 showed better irradiation resistance than alloy 625, 625DA and alloy 625Plus based on the susceptibility of formation of long range order phase. Alloy 625 and alloy 625DA showed the poorest performance in phase stability.
    - Long range ordered phase (Ni_2Cr) was observed in all these alloys after proton irradiation. The precipitates were larger in alloy 725 and alloy 690 compared to alloy 625 and alloy 625Plus. The density of the precipitates was higher in alloy 625 and alloy 625DA compared to alloy 625Plus and alloy 725.
    - No voids were observed in these alloys due to the relatively low dose level.
    - Faulted loops were observed in all the alloys. Larger size and lower density of loops were observed in alloy 690 compared to alloy 625Plus, 625DA, alloy 625 and alloy 725. The stacking fault energy directly controlled the size of faulted loops.
- Voids were observed in alloy 316L and alloy 310.
- Alloy T92 showed better irradiation tolerance as measured by irradiation hardening response
    - Irradiation hardening was noticed in all alloys. The highest irradiation induced hardening was observed in the group of austenitic stainless steel alloy 800, 316L. Moderate radiation hardening was observed in alloy 625, 625DA, 725 and 625Plus.
    - The dispersed barrier hardening model failed to describe the irradiation hardening behavior when the dislocation loops and precipitates were coupled in the model. Both calculations with simple rule mixture and root sum square assumption deviated from the experiment values.

- Evaluation of IASCC behavior of the nickel-base alloys, alloy 625Plus, alloy 625DA, alloy 725, and alloy 625, in both BWR NWC and PWR primary water was made:
    - For high strength alloys, alloy 625DA was the most susceptible to IASCC while alloy 725 is the least susceptible. Alloy 625Plus was in the middle range.
    - For low strength alloy, alloy 625 was much more susceptible to IASCC than a reference alloy (austenitic stainless steel Type 304) in BWR NWC environment.
    - All high strength alloys had higher IASCC susceptibility in BWR NWC while Alloy 625 had a higher IASCC susceptibility in PWR primary water.
- Radiation induced microstructural changes play an important role in cracking susceptibility, however no single one feature can be identified as the major cause. Alloy 625DA suffered the most significant microstructure changes after irradiation, thus it had the worst IASCC susceptibility in LWR environment.
- Radiation-induced segregation was proven not as a major effect to the IASCC susceptibility to nickel-base alloys. Alloy 725 has the most significant RIS changes among all nickel base alloys, but it had the best IASCC resistance in LWR environment.

From the irradiation hardening perspective, alloy T92 showed the lowest irradiation hardening. Alloy 725 exhibited the better phase stability in the group of high strength alloys examined so far. Alloy 310L and alloy 316L show poor void swelling resistance. Alloy 625 and 625DA show high susceptibility to the formation of long range order phase.

All nickel base alloys, alloy 625Plus, alloy 625DA, alloy 725, and alloy 625 exhibited large increases in IASCC susceptibility following proton irradiation to 5 dpa in both BWR NWC and PWR primary water environments. In all cases, cracking was more severe in BWR NWC than in PWR primary water. Although no microstructure feature has been identified as the cause of the poor IASCC resistance, alloy 625DA had the highest susceptibility to IASCC and the exhibited the greatest changes in all microstructure features following irradiation.

ACKNOWLEDGMENTS

This research was subcontracted through Oak Ridge National Laboratory (ORNL), in support of the Light Water Reactor Sustainability (LWRS) Program Research and Development (R&D) effort, sponsored by the U.S. Department of Energy (DOE), Office of Nuclear Energy (NE). We gratefully acknowledge the support provided by Richard A. Reister of DOE-NE, Federal Project Director of Light Water Reactor Deployment; Kathryn A. McCarthy of Idaho National Laboratory (INL), Director of the LWRS Program Technical Integration Office (TIO); Donald L. Williams, Jr. of ORNL, Deputy Director of the LWRS Program TIO; Cathy J. Barnard of INL, Program Manager of the LWRS Program TIO; and Keith J. Leonard of ORNL, Lead of Materials Aging and Degradation R&D Pathway of the LWRS Program.

The authors are grateful to Raj Pathania (Electric Power Research Institute [EPRI]) and Larry Nelson (JLN Consulting) for their managing and coordinating the Advanced Radiation Resistant Materials (ARRM) program; Martin Morra (General Electric [GE] Global Research Center), David Sandusky (retiree of GE Nuclear Energy), Benjamin Sutton (EPRI), and Lizhen Tan (ORNL) for helpful discussions and sharing the alloys.

REFERENCES

[1] P. Scott. A review of irradiation assisted stress corrosion cracking, J. Nucl. Mater. 211 (1994) 101-122.

[2] E. Kenik, R. Jones, G. Bell. Irradiation-assisted stress corrosion cracking, J. Nucl. Mater. 212 (1994) 52-59.

[3] G.S. Was, S.M. Bruemmer. Effects of irradiation on intergranular stress corrosion cracking, J. Nucl. Mater. 216 (1994) 326-347.

[4] J. Busby, G. Was, E. Kenik. Isolating the effect of radiation-induced segregation in irradiation-assisted stress corrosion cracking of austenitic stainless steels, J. Nucl. Mater. 302 (2002) 20-40.

[5] G. Was, P. Ampornrat, G. Gupta, S. Teysseyre, E. West, T. Allen, K. Sridharan, L. Tan, Y. Chen, X. Ren. Corrosion and stress corrosion cracking in supercritical water, J. Nucl. Mater. 371 (2007) 176-201.

[6] S.J. Zinkle, G. Was. Materials challenges in nuclear energy, Acta Mater. 61 (2013) 735-758.

[7] G. Was, Y. Ashida, K. Stephenson, A. Flick, P. Andresen. Identifying Mechanisms and Mitigation Strategies for Irradiation Assisted Stress Corrosion Cracking of Austenitic Steels in LWR Core Components, EPRI 3002003105 (2014).

[8] S. Bruemmer. New Issues Concerning Radiation-Induced Material Changes and Irradiation-Assisted Stress Corrosion Cracking in Light Water Reactors. Proc. 10th Int. Conf. Environmental Degradation of Materials in Nuclear Power Systems—Water Reactors (Houston, TX: NACE, 2002), 2002.

[9] O. Chopra, A. Rao. A review of irradiation effects on LWR core internal materials–Neutron embrittlement, J. Nucl. Mater. 412 (2011) 195-208.

[10] O. Chopra, A. Rao. A review of irradiation effects on LWR core internal materials–IASCC susceptibility and crack growth rates of austenitic stainless steels, J. Nucl. Mater. 409 (2011) 235-256.

[11] P. Andresen, F. Garner, J. Gorman, S. Maloy, J. Nelson, L. Tan, M. Toloczko, G. Was. Critical Issues Report and Roadmap for the Advanced Radiation-Resistant Materials Program 1026482, EPRI 1026482 (2012).

[12] F.A. Garner, B.M. Oliver, L.R. Greenwood, D.J. Edwards, S.M. Bruemmer, M.L. Grossbeck. Generation and retention of helium and hydrogen in austenitic steels irradiated in a variety of LWR and test reactor spectral environments. Pacific Northwest National Laboratory (PNNL), Richland, WA (US), 2002.

[13] M. Miglin, H. Domian. Microstructure and stress corrosion resistance of alloys X750, 718, and A286 in light water reactor environments, Journal of materials engineering 9 (1987) 113-132.

[14] J.P.B. J.F.Ziegler. SRIM 2013 Program, IBM Corporation, Yorktown ,NY.

[15] G. Gupta, Z. Jiao, A. Ham, J. Busby, G. Was. Microstructural evolution of proton irradiated T91, J. Nucl. Mater. 351 (2006) 162-173.

[16] P. Lin, G. Palumbo, U. Erb, K. Aust. Influence of grain boundary character distribution on sensitization and intergranular corrosion of alloy 600, Scripta Metallurgica et materialia 33 (1995) 1387-1392.

[17] R. Cozar, A. Pineau. Morphology of y'and y" precipitates and thermal stability of inconel 718 type alloys, Metall. Trans. 4 (1973) 47-59.

[18] S. Hong, W. Chen, T. Wang. A diffraction study of the γ'' phase in INCONEL 718 superalloy, Metall. Mater. Trans. A 32 (2001) 1887-1901.

[19] T. Maki, K. Tsuzaki, I. Tamura. The morphology of microstructure composed of lath martensites in steels, Trans. Iron Steel Inst.Jap 20 (1980) 207-214.

[20] G. Krauss, A. Marder. The morphology of martensite in iron alloys, Metall. Trans. 2 (1971) 2343-2357.

[21] S. Morito, H. Tanaka, R. Konishi, T. Furuhara, T. Maki. The morphology and crystallography of lath martensite in Fe-C alloys, Acta Mater. 51 (2003) 1789-1799.

[22] S. Morito, X. Huang, T. Furuhara, T. Maki, N. Hansen. The morphology and crystallography of lath martensite in alloy steels, Acta Mater. 54 (2006) 5323-5331.

[23] Z. Jiao, G. Was. The role of irradiated microstructure in the localized deformation of austenitic stainless steels, J. Nucl. Mater. 407 (2010) 34-43.
[24] Z. Jiao, J. Busby, G. Was. Deformation microstructure of proton-irradiated stainless steels, J. Nucl. Mater. 361 (2007) 218-227.
[25] G.S. Was. Fundamentals of radiation materials science: metals and alloys, Springer Science & Business Media, 2007.
[26] G. Young, D. Eno. Long range ordering in model Ni-Cr-X alloys, (2015).
[27] M. Sundararaman, L. Kumar, G.E. Prasad, P. Mukhopadhyay, S. Banerjee. Precipitation of an intermetallic phase with Pt2Mo-type structure in alloy 625, Metall. Mater. Trans. A 30 (1999) 41-52.
[28] C. Thomas, P. Tait. The performance of Alloy 625 in long-term intermediate temperature applications, Int.J .Pres. Ves. Pip. 59 (1994) 41-49.
[29] G.A. Young, J.D. Tucker, D.R. Eno. THE KINETICS OF LONG RANGE ORDERING IN NI-CR AND NI-CR-FE ALLOYS.
[30] A. Marucco. Atomic ordering in the Ni Cr Fe system, Mater. Sci. Eng. A 189 (1994) 267-276.
[31] H. Tawancy, F. Alyousef. Effect of long-range ordering in a Ni–Mo alloy on its mechanical properties and corrosion resistance, J. Mater. Sci. 42 (2007) 9121-9124.
[32] R. Bajaj, W. Mills, M. Lebo, B. Hyatt, M. Burke. Irradiation-assisted stress corrosion cracking of HTH Alloy X-750 and Alloy 625. Seventh International Symposium on Environmental Degradation of Materials in Nuclear Power Systems--Water Reactors., vol. 2, 1995. p.1093-1107.
[33] C. Cawthorne, E. Fulton. Voids in irradiated stainless steel, (1967).
[34] F. Carrette, M. Lafont, G. Chatainier, L. Guinard, B. Pieraggi. Analysis and TEM examination of corrosion scales grown on Alloy 690 exposed to pressurized water at 325 C, Surface and interface Analysis 34 (2002) 135-138.
[35] A. Machet, A. Galtayries, S. Zanna, L. Klein, V. Maurice, P. Jolivet, M. Foucault, P. Combrade, P. Scott, P. Marcus. XPS and STM study of the growth and structure of passive films in high temperature water on a nickel-base alloy, Electrochimica Acta 49 (2004) 3957-3964.
[36] L. Marchetti, S. Perrin, Y. Wouters, F. Martin, M. Pijolat. Photoelectrochemical study of nickel base alloys oxide films formed at high temperature and high pressure water, Electrochimica Acta 55 (2010) 5384-5392.
[37] M. Sennour, L. Marchetti, F. Martin, S. Perrin, R. Molins, M. Pijolat. A detailed TEM and SEM study of Ni-base alloys oxide scales formed in primary conditions of pressurized water reactor, J. Nucl. Mater. 402 (2010) 147-156.
[38] L. Marchetti-Sillans. PhD thesis (2007).
[39] J. Tien, S. Copley. The effect of uniaxial stress on the periodic morphology of coherent gamma prime precipitates in nickel-base superalloy crystals, Metall. Trans. 2 (1971) 215-219.
[40] J. Oblak, D. Paulonis, D. Duvall. Coherency strengthening in Ni base alloys hardened by DO22 γ' precipitates, Metall. Trans. 5 (1974) 143-153.
[41] T. Eto, A. Sato, T. Mori. Stress-oriented precipitation of GP Zones and θ' in an Al Cu alloy, Acta Metall. 26 (1978) 499-508.
[42] T. Miyazaki, K. Nakamura, H. Mori. Experimental and theoretical investigations on morphological changes of γ' precipitates in Ni-Al single crystals during uniaxial stress-annealing, J. Mater. Sci. 14 (1979) 1827-1837.
[43] B. Skrotzki, G. Shiflet, E. Starke Jr. On the effect of stress on nucleation and growth of precipitates in an Al-Cu-Mg-Ag alloy, Metall. Mater. Trans. A 27 (1996) 3431-3444.
[44] A. Zhu, E. Starke. Stress aging of Al–xCu alloys: experiments, Acta Mater. 49 (2001) 2285-2295.
[45] R. Doherty. Diffusive phase transformations in the solid state, Physical metallurgy 2 (1996) 1456-1458.

[46] J.D. Eshelby. The determination of the elastic field of an ellipsoidal inclusion, and related problems. Proceedings of the Royal Society of London A: Mathematical, Physical and Engineering Sciences, vol. 241: The Royal Society, 1957. p.376-396.
[47] S. Mannan, F. Veltry. Time-Tempearature-Trasnformation Diagram of Alloy 725, TMS, 2001.
[48] R.L. Fleischer. Solution hardening by tetragonal dist ortions: Application to irradiation hardening in FCC crystals, Acta Metall. 10 (1962) 835-842.
[49] J. Eshelby. The elastic field outside an ellipsoidal inclusion. Proceedings of the Royal Society of London A: Mathematical, Physical and Engineering Sciences, vol. 252: The Royal Society, 1959. p.561-569.
[50] L. Tan, J.T. Busby. Formulating the strength factor α for improved predictability of radiation hardening, J. Nucl. Mater. 465 (2015) 724-730.
[51] E. Orowan. Internal stress in metals and alloys, The Institute of Metals, London (1948) p451.
[52] R.O. Scattergood, D.J. Bacon. The Orowan mechanism in anisotropic crystals, Philos. Mag. 31 (1975) 179-198.
[53] A. Foreman, M. Makin. Dislocation movement through random arrays of obstacles, Philos. Mag. 14 (1966) 911-924.
[54] S. UKAI, S. MIZUTA, M. FUJIWARA, T. OKUDA, T. KOBAYASHI. Development of 9Cr-ODS martensitic steel claddings for fuel pins by means of ferrite to austenite phase transformation, Journal of Nuclear Science and Technology 39 (2002) 778-788.
[55] T. Gladman. Precipitation hardening in metals, Mater. Sci.Technol. 15 (1999) 30-36.
[56] B. Singh, A. Foreman, H. Trinkaus. Radiation hardening revisited: role of intracascade clustering, J. Nucl. Mater. 249 (1997) 103-115.